Hydraulic performance of oscillating water column structures as anti-reflection devices to reduce harbour agitation

Coastal Engineering 165 (2021) 103837

Contents lists available at ScienceDirect

Coastal Engineering

journal homepage: http://www.elsevier.com/locate/coastaleng

Hydraulic performance of oscillating water column structures as anti-reflection devices to reduce harbour agitation

Irene Simonetti *, Lorenzo Cappietti

LABIMA - Dept. of Civil and Environmental Engineering, University of Florence, Via di S. Marta 3, 50139, Florence, Italy

ARTICLE INFO

Keywords:
Anti-reflection devices
Vertical wall harbour structures
Reduce harbour agitation
Oscillating water column
Reflection coefficients
Empirical formulae

ABSTRACT

This paper aims at assessing the effectiveness of an oscillating water column device, generally conceived and studied as a wave energy converter, as an anti-reflective system to be integrated into vertical wall harbour structures. The wave-structure interaction is studied with simulations carried out in a numerical wave tank, implemented in the computational fluid dynamics environment OpenFOAM®. Reflected and radiated wave components are decomposed and the interaction between these components is studied. A quasi-standing wave field is present in front of the structure. The effect of design parameters and hydrodynamic conditions on the reflection properties and on the wave field in front of the structure is discussed. Results are analysed in terms of dimensionless parameters and original empirical formulae to predict the wave reflection are given. Minimum reflection coefficients (including both properly reflected and radiated waves) around 15% are found, suggesting that the OWC could efficiently be used to reduce wave agitation in front of vertical wall harbour structures. The reflection coefficient is primarily influenced by the ratio of the camber length W to the incident wavelength L, with minimum values for W/L = 0.1–0.17. Minimum values of the ratio of the quasi-antinode height to the incident wave height around 1.1 are found.

1. Introduction and motivations

Wave reflection at harbour structures contributes to disturb harbour tranquillity, affecting the navigability of entrance canals and compromising the safety of manoeuvring, berthing and loading operations inside the harbour. Even if wave reflection is relatively limited for rubble-mound structures if compared to vertical-wall structures, for deep water applications the use of the vertical-wall structures is often preferred due to economic reasons. Moreover, vertical-wall structures limit the footprint of the moorings, allowing a more effective design of berthing structures. The present trend in vessels design for global trades shows an increase of the vessels size, with higher drafts, in turn imposing greater depths of the harbours. In this framework, the use of berthing structures of the vertical-wall type seems to be the most suited approach. Reducing wave reflection at such structures is, therefore, a relevant aim. Over the years, several low-reflectivity structures have been proposed in the literature to deal with this specific problem, as reviewed in Oumeraci and Kim (2008) and Huang et al. (2011).

The earliest studies on the effectiveness of slotted vertical perforated-walls are those by Jarlan (1961). Fugazza and Natale (1992) demonstrated that resonance phenomenon takes place inside perforated breakwaters with a single chamber for ratios of the structure length to the incident wavelength $W/L = 0.25$. In this condition, caissons have the maximum efficiency in limiting the wave reflection due to destructive interference phenomena. Vertical perforated-walls are often also adopted as the frontal or internal wall of caisson breakwaters embodying multiple chambers. Lee and Shin (2014) comparatively tested single and double camber perforated caissons, obtaining the lowest reflection coefficients (around 0.3) for a ratio of the structure length to the incident wavelength W/L equal to 0.1–0.2. Such work suggested that using multiple perforated walls may lower the optimal W/L ratio. In more recent studies by Neelamani et al. (2017), several slotted-walls in series were tested, finding minimum reflection coefficients around 0.35 when using three walls in series with a 50% porosity (for W/L = ~0.18). Garrido et al. (2010) and Gonzalez-Escriva and Medina (2012) proposed an innovative multi-cell circuit to reduce long resonance waves inside harbours, finding reflection coefficients between 0.6 and 0.9 for the shorter wave cases. Ciocan et al. (2017) and López et al. (2018) proposed and tested the multi-chamber LOWREB structure, having reflection coefficients of 0.3–0.7 (with minimum values for W/L = 0.15).

* Corresponding author.
E-mail address: irene.simonetti@unifi.it (I. Simonetti).

https://doi.org/10.1016/j.coastaleng.2020.103837
Received 1 September 2020; Received in revised form 13 December 2020; Accepted 22 December 2020
Available online 24 December 2020

Caissons with internal rubble mound slopes were also proposed to reduce inner harbour agitation. Theocharis et al. (2011) verified by means of field tests that wave absorbing quay walls with a rock-armoured slope are able to reduce the wave height up to 20–30%. Also for such type of structure, minimum reflection coefficients around 0.3 were obtained from laboratory tests (Altomare et al., 2013; Altomare and Gironella, 2014).

Combined caissons, i.e. caissons with a perforated concrete seawall and an internal rubble mound slope, have also been proposed and applied as an alternative to reduce the horizontal space required by the structure to dissipate the incident wave energy (Cavallaro et al., 2009; Faraci et al., 2015). In the experimental study of Faraci et al. (2015), reflection coefficients lower than 0.4 were found for relative lengths of the structure $W/L > 0.15$.

In a perforated/slotted breakwater, as well as in caissons with an internal rubble mound or combined caissons, part of the incident wave energy is reflected at the perforated seaward wall and part of it is transmitted inside the caisson, where it is partially dissipated due to different phenomena, e.g. turbulence, friction losses, vortices and resonance effects. The main parameters affecting the performance of such structures are the structure porosity and the length of the wave absorbing chamber. For a structure with an internal rubble mound, the wave energy dissipation is mainly due to the turbulent flows into the rubble mound voids (Altomare and Gironella, 2014). The aforementioned low-reflectivity structures passively dissipate the energy, without attempting to recover it into useable forms.

The so-called Oscillating Water Column (OWC) concept, commonly conceived as a Wave Energy Converter (WEC) (Falcão and Henriques, 2016), could also represent a possible way to absorb the incident energy and, consequently, to decrease the reflection. The OWC structure is a hollow chamber, open below the still water level, where the wave motion drives a heave-direction oscillation of the inner mass of water. The wave-induced motion of the water column alternatively expands and compresses an upstanding volume of air, forming an oscillatory airflow which drives a self-rectifying air turbine installed in a vent, which connects the internal part of the device to the atmosphere. Finally, electrical energy is generated by an electrical generator driven by the air turbine.

From its first developments around 1970 (Masuda, 1971) to the full-scale prototype installations (e.g. Torre-Enciso et al., 2009; Arena et al., 2014; Falcão et al., 2020), the OWC technology has been widely studied to maximize the energy harvesting under specific wave conditions (Ning et al., 2016; He et al., 2016; Simonetti et al., 2017; Elhanafi et al., 2017a; López et al., 2019; Zabihi et al., 2019). As for any WEC, one of the main issues for the diffusion of OWC devices is that, compared to other renewable energy extraction technologies, e.g. wind and solar, the overall cost of wave energy conversion is too high to be competitive on the market. The cost of building and installing the device constitutes a relevant part of the overall expenses. As a solution to decrease costs, the possibility of building OWCs as hybrid structures integrated into coastal infrastructures, e.g. breakwaters, is getting growing attention. A review of the possible innovative solutions incorporating WEC technologies, including OWCs, into harbour breakwaters is provided by Mustapa et al. (2017) and Vicinanza et al. (2019), which concluded that research efforts should be oriented towards the understanding of the hydraulic performance and reliability of such innovative structures, to further demonstrate their potential.

In 2016, Naty et al. performed a structural-economic feasibility study for integrating an OWC device into a harbour breakwater in the Mediterranean context (Naty et al., 2016), optimizing the system from the wave energy extraction point of view. Despite a quite long payback period of investment (19 years), the authors concluded that integrating OWCs into coastal structures could be a promising possibility. Viviano et al. (2016, 2019) performed large scale experiments on an OWC device, estimating a minimum reflection coefficient of around 0.2 when the length of the OWC chamber relative to the incident wavelength (W/L) is around 0.1–0.15. Howe and Nader (2017) compared the wave energy extraction performance of an isolated OWC with that of an OWC integrated into a breakwater, finding a significant increase of the power absorption for the integrated case.

Studies that specifically investigate the effectiveness of OWCs as anti-reflection devices to be incorporated in vertical wall harbour structures are quite limited. He and Huang (2016) performed laboratory tests on a small-scale pile-supported OWC to prove the suitability of such structure to reduce wave reflection from vertical walls, concluding that OWCs can be as effective as slotted-barrier caisson to reduce wave reflection (with minimum reflection coefficients of around 0.3, obtained for $W/L = 0.2$).

An OWC structure could reduce wave reflection in front of a vertical wall since it absorbs part of the incident energy in the form of pneumatic energy of the reciprocating airflow. Moreover, other dissipating mechanisms, such as water vortex shedding taking place at the OWC front wall, may represent a further way to reduce the reflected wave energy (He and Huang, 2016; Elhanafi et al., 2016a). However, while absorbing part of the incident wave energy, the time-varying air pressure acting on the free surface of the water inside OWC implies that the device necessarily radiates waves toward the exterior (Sarmento and Falcão, 1985; Falnes, 2002). The wave field in front of the OWC depends on the interaction between the incident, the reflected and the radiated waves, assuming that the device is integrated into a bottom standing breakwater and therefore no energy is transmitted underneath or behind it. Such interaction may be either constructive or destructive.

The wave field in front of on OWC structure has been scarcely investigated, e.g. in Scarpetta et al. (2017) and Gurnari et al. (2020). In such works, the partial reflection wave field in front of a U-OWC was studied, but reflection coefficients were not provided.

The present work aims to contribute to the current knowledge on the effectiveness of an OWC, embodied in quay walls or harbour breakwaters, as an alternative to reduce the wave reflection at vertical wall structures. The objective of this work is to study the wave field in front of the OWC device and its sensitivity to the variation of the design parameters, highlighting the contribution of both reflected and radiated waves. Part of the methodology here adopted was presented for the first time by Cappietti and Simonetti (2018). This work is an extension of such previous study, providing a larger dataset of tested geometries and wave conditions. Consequently, a more comprehensive analysis of reflection coefficients and water agitation in front of the structure is also provided, leading to the development of empirical formulae to predict the most relevant variables from the harbour engineering practice point of view. To the authors' knowledge, no other previous study specifically attempted to quantify wave radiation from OWCs conceived as anti-reflection structures integrated into harbour breakwaters.

The remainder of the paper is structured as follows: the set-up of the Numerical Wave Tank (NWT) used to study the wave-structure interaction is presented, with a focus on the methodology to separate incident, reflected and radiated waves and on the validation with laboratory data. The effect of the OWC parameters and the hydrodynamic conditions on the reflection properties of the structure is analysed and empirical prediction formulae based on dimensional analysis are developed. Results are then discussed, also with reference to the performance of more consolidated wave-damping structures. Finally, concluding remarks are given.

2. Methodology

The work is based on numerical modelling, performed in a NWT based on Computational Fluid Dynamics (CFD). Numerical simulations are carried out using the OpenFOAM® software package. The flow equations of the two-phase (water and air) flow are introduced at first, with emphasis on the turbulence model, the computational domain and the numerical set-up. The methodology applied to decompose the reflected and the radiated wave fields based on numerical simulations was

presented for the first time in Cappietti and Simonetti (2018) and is briefly recalled in this section for sake of clarity, together with a description of the new set of simulations used to examine the characteristics of the wave field in the proximity of the structure and of the procedure applied to develop the original prediction formulae based on the available data (*section 2.2*). Subsequently, a more comprehensive validation than that provided in Cappietti and Simonetti (2018) is discussed on the base of model results in comparison with laboratory data available in the literature.

2.1. The numerical wave tank

The OWC device is simulated in a two-dimensional NWT. The calculations are performed by solving mass conservation, Eq. (1), and Reynolds Averaged Navier-Stokes (RANS) equations, Eq. (2), for two incompressible phases by using the *interFoam* solver of the OpenFOAM® software package.

$$\nabla \cdot U = 0 \tag{1}$$

$$\frac{\partial \rho U}{\partial t} + \nabla \cdot (\rho U \otimes U) - \nabla \cdot \left(\mu_{eff} \nabla U\right) = -\nabla p - g \cdot x \nabla \rho + \nabla U \cdot \nabla \mu_{eff} + \sigma \kappa \nabla \gamma \tag{2}$$

where U is the fluid velocity vector, ρ is the fluid density, μ_{eff} is the efficient dynamic viscosity (defined as $\mu_{eff} = \mu + \mu_t$, with μ being the molecular dynamic viscosity and μ_t being the turbulent viscosity), p is the pressure, g is the vector of acceleration of gravity, x is the position vector, σ is the surface tension coefficient, κ is the interface curvature. The Volume of Fluid (VOF) method (Hirt and Nichols, 1981) is used. In the VOF method, γ is the volume phase fraction, i.e. the quantity of water per unit volume of each cell ($0 \leq \gamma \leq 1$, with values 0 and 1 for the regions containing only air or only water, respectively). A transport equation for γ is solved, Eq. (3):

$$\frac{\partial \gamma}{\partial t} + \nabla \cdot (\mathrm{U}\gamma) + \nabla \cdot (\mathrm{U}_r \gamma (1-\gamma)) = 0 \tag{3}$$

where U_r is an artificial velocity used to limit the smearing of the air-water interface. The relaxation zone technique of *waves2Foam* (Jacobsen et al., 2012) is used for waves generation/absorption at the inlet boundary. With this approach, the boundary condition used to introduce waves at the inlet is specified according to the selected wave theory. Inside the relaxation zone, velocity components and water surface elevation are imposed as a weighted average of analytical and solved solutions, Eq. (4) and Eq. (5).

$$\alpha_R = 1 - \frac{e^{\left(\chi_R^{3.5}\right)} - 1}{e^{(1)} - 1} \tag{4}$$

$$\Phi = \alpha_R \Phi_{\text{computed}} + (1 - \alpha_R)\Phi_{\text{target}} \tag{5}$$

where Φ indicates either γ or U and χ_R is defined to have $\alpha_R = 1$ at the end of the relaxation zone.

In the present work, the k-ω SST (*Shear Stress Transport*) turbulence model is used. The k-ω SST model, originally proposed by Menter (1992), is a two-equation eddy-viscosity model which combines the k-ω and the k-ε models: a blending function activates the k-ω model near the wall and the k-ε model in the free stream. In recent years, such a turbulence model has been widely applied in CFD-based numerical NWT used to simulate WECs, as thoroughly reviewed by Windt et al. (2018). For the specific case of simulating the nearfield of OWC systems, the k-ω SST turbulence model was shown to have satisfactory performance, in terms of validation with laboratory results (Elhanafi et al., 2016b, 2017b; Iturrioz et al., 2015). In this work, a modified version of the k-ω SST turbulence model specifically developed to ensure a stable long-term wave propagation over relatively extended domains is used, i.e. the so-called *buoyancy-modified* k-ω SST model, presented by Devolder et al. (2017). Indeed, particularly for the case of high steepness waves, a relevant wave damping in RANS simulations has been reported in the literature (Devolder et al., 2017, 2018; Paulsen et al., 2014; Larsen and Fuhrman, 2018), due to an exponential growth of turbulent kinetic energy density and eddy viscosity in the entire flow region under a surface wave which takes place in two equations turbulence models (Larsen and Fuhrman, 2018). Although the *buoyancy-modified* k-ω SST model significantly reduces the unphysical wave damping and it is judged to be sufficiently predictive for the purposes of the present work (as also discussed in Appendix A), it is worth to mention that the use of the buoyancy-modification term alone does not allow to achieve formal stability in the turbulence closure, as recently discussed in Fuhrman and Larsen (2019).

The computational domain of the two-dimensional NWT has total length and height equal to those of the wave-current flume of the Laboratory of Maritime Engineering of Florence University (LABIMA), i.e. respectively 37 m and 0.8 m. The inlet relaxation zone has a length of 4 m (corresponding to 1.7–4·L for the range of tested waves, being L the wavelength) to allow for a proper generation/absorption of the incident wave. The OWC structure is located at the end of the NWT (Fig. 1), therefore a relaxation zone is not used at the outlet (indeed, the quantification of the wave reflection from the structure is one of the aims of this work). No-slip boundary conditions are used at the bottom of the NWT and on the OWC sidewalls. The water surface is set as an atmospheric pressure boundary. Velocity components and water surface elevations at the inlet are defined to introduce regular waves with *waves2Foam*. The mesh is refined in the free surface zone, with a resolution of around 20 cells per wave height H and a maximum cells aspect ratio equal to 2 (Fig. 1). The resulting mesh of the whole NWT has a size of approximately 400′000 cells. The mesh resolution has been chosen based on sensitivity tests aimed at ensuring substantial mesh independence for the wave propagation in the NWT, as specifically discussed in Cappietti and Simonetti (2018).

The PIMPLE algorithm, a hybrid version of the PISO and the SIMPLE algorithms (Jasak, 1996), is used for the coupling of the equations in the pressure-velocity system. The time step is dynamically adjusted to maintain a value of the Courant number $Co < 0.2$ and a value of Co at the air-water interface $\alpha Co < 0.2$. The numerical schemes used for the discretization of the time derivatives are second-order accurate, blended with a first-order Euler scheme to improve stability (*CrankNicolson* scheme in OpenFOAM®). Time step and blending factor of the *CrankNicolson* scheme have been chosen consequently to the sensitivity tests documented in Appendix A.

A standard finite volume discretization of Gaussian integration is applied to gradient operators, with a central differencing scheme for cell-centre to cell-face interpolation. The convection term in momentum equation is discretized with a central difference interpolation scheme. The convection term in the transport equation of the phase fraction γ uses the Monotone Upwind Scheme for Scalar Conservation Laws (MUSCL) interpolation scheme. A generalized Geometric-Algebraic Multi-Grid solver (GAMG) is used to solve the discretized system of equations.

2.2. Decomposition of the reflected and the radiated wave field and water agitation in front of the structure

The NWT is used to examine separately the reflected and the radiated wave components by applying the following methodology (Fig. 2): in a 1st step, a 110 wave periods (T)-long numerical simulation is performed, with a 20T-long initial wave generation interval. The generated wave train propagates in the NWT, reaches the OWC structure, is reflected and propagates back towards the wave generation boundary. The wave train moving back to the generation boundary propagates in still water and includes both the properly reflected and the radiated waves (called hereafter *total reflected wave*, with height H_{rr}). Therefore, it is possible to separate the incident and the total reflected wave trains in any selected

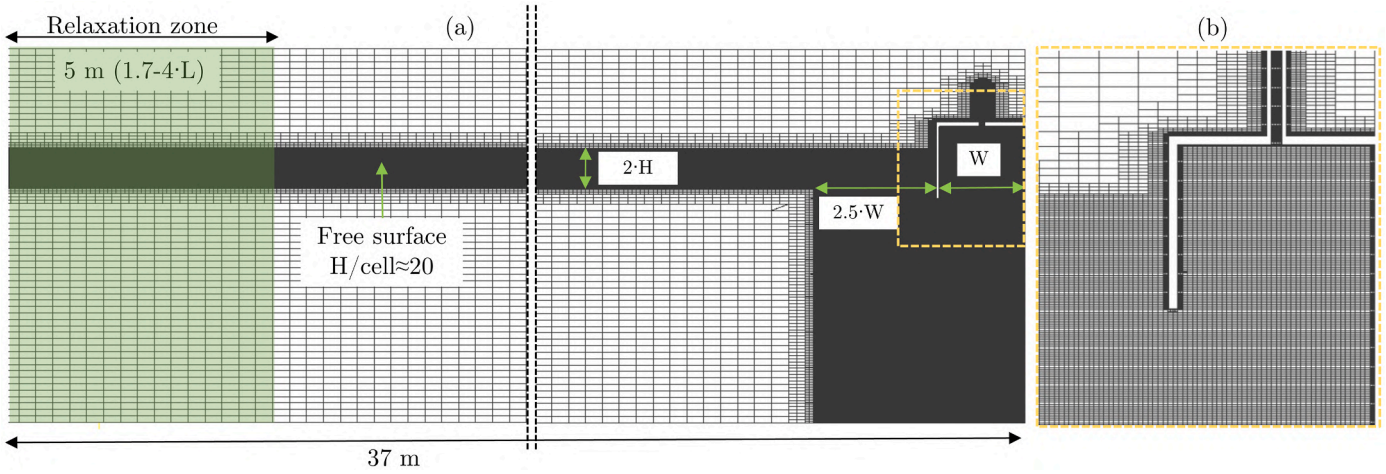

Fig. 1. Numerical Wave Tank (NWT) (a), close-up of the computational mesh in the region around the OWC structure (b). *L*: incident wavelength, *H*: incident wave height, *W*: chamber length.

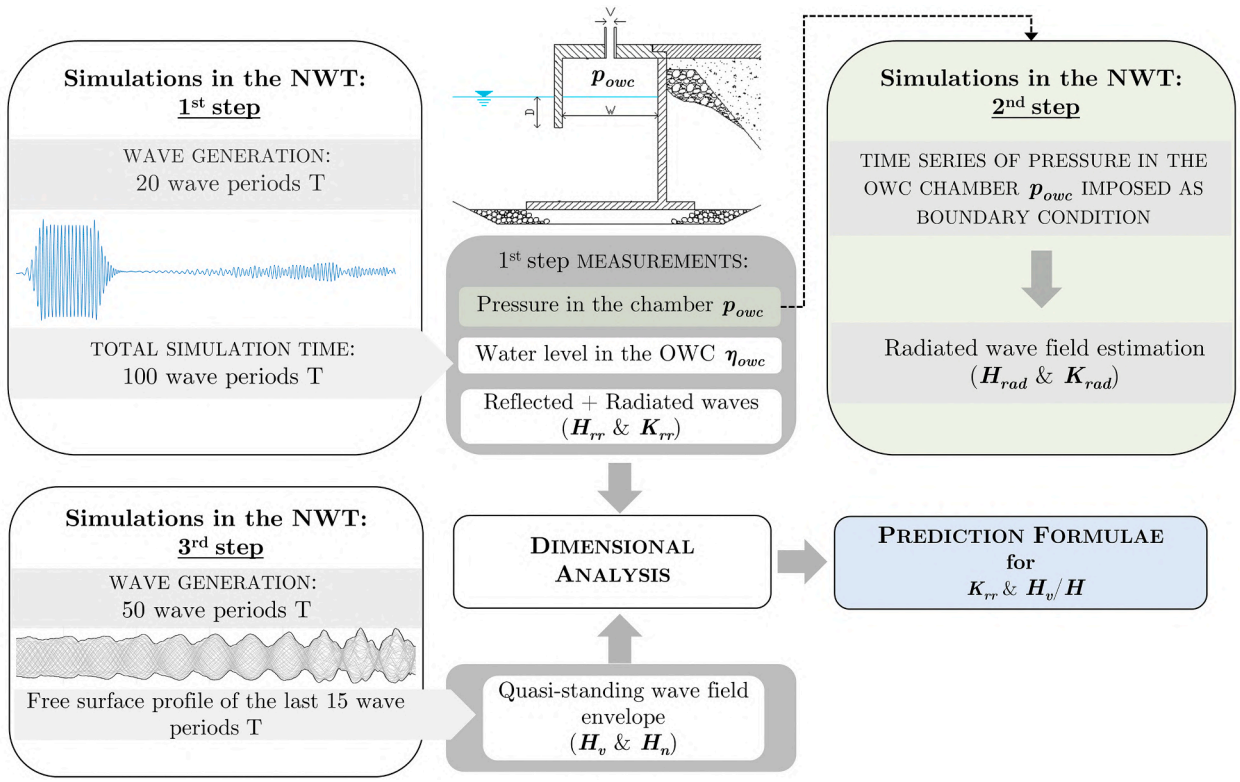

Fig. 2. Workflow of the methodology used to estimate the total reflection coefficient K_{rr} (1st step simulations), to decompose the properly reflected and radiated waves (2nd step simulations) and to examine the global agitation in front of the structure (3rd step simulations) in the NWT.

location along the NWT. The total reflected wave field, and the corresponding total reflection coefficient K_{rr}, can be directly measured through the zero-crossing analysis, without using spectral methods for separating the incoming and the outgoing wave fields (Mansard and Funke, 1980; Goda and Suzuki, 1977). The time series of air pressure in the OWC (p_{owc}) obtained in the 1st step simulations is then imposed as an input for the simulations of the 2nd step. The wave generated in the NWT because of the time-varying pressure acting inside the OWC chamber, H_{rad}, is measured (i.e. the radiated wave field is explicitly quantified). A sensitivity analysis is performed on the time window used for the analysis in order to ensure that this parameter does not significantly affect the results. Shifting the start and the end times selected for the analysis of $\pm 2T$ results in maximum relative differences in the estimated quantities lower than 7%, which is considered acceptable.

As aforementioned, the methodology used to decompose the properly reflected and the radiated wave components (i.e. 1st and 2nd step simulations in Fig. 2) has been presented for the first time in Cappietti and Simonetti (2018). The present work substantially enlarges the range of conditions tested with such methodology. Furthermore, to provide a quantification of the global agitation in front of the vertical-wall structure embodying the OWC, considering the interaction between the reflected plus radiated and the incident wave fields, an additional set of simulations has been added in this work (denoted as 3rd step simulations in Fig. 2). The following procedure is used: (i) 50*T*-long simulations are

performed in a 20L-long NWT, generating waves from the inlet relaxation zone (having a 4L-length) for the whole simulation time; (ii) profiles of the free surface along the NWT are collected at a 1/10T interval; (iii) the free surface profiles during the last 15T seconds of the simulation are overlapped, and the envelope of the free surface wave field is obtained. The quasi-antinode (H_v) and the quasi-node (H_n) heights are estimated.

The data obtained from the simulation of 1st, 2nd and 3rd step are examined based on dimensional analysis, leading to the formulation of prediction formulae for K_{rr} and H_v/H.

2.3. Validation of the numerical wave tank

The comparison between the numerical model predictions and the results of laboratory-scale tests carried out in the wave-current flume of Florence University (Simonetti et al., 2017; Crema et al., 2015) shows relatively good performance of the numerical model in predicting the quantities of interest (Fig. 3). The relative error between the experiments and the NWT results is lower than 15% for the pressure (p_{owc}) and the water level (η_{owc}) inside the OWC chamber, which is considered acceptable. Moreover, considering more specifically the value of the reflection coefficient K_{rr}, the results of the numerical model are compared with experimental data available in the literature (He and Huang, 2016). When testing the same structure geometry and hydrodynamic conditions, K_{rr} values obtained from numerical simulations in this work match closely those by He and Huang (2016) (Fig. 4). The agreement is satisfactory also considering additional parameters related to the OWC functioning, i.e. the pressure coefficient C_p, defined as in Eq. (11), and the Capture Width ratio CW, defined in Eq. (12).

3. Tested OWC geometries, wave conditions and dimensional analysis

The OWC structure studied in this work consists of a rectangular-shaped hollow chamber, conceived to be embedded into a vertical-wall harbour structure. A water depth of $h = 9$ m is considered, with a fixed value of the OWC freeboard $Fc = 1.5$ m, as typical harbour depth and deck level for a marina harbour. Values of the chamber length W varying between 2 and 4 m and front wall draught D of 1–2.5 m are tested. On the top of the chamber, an aperture with a length V = 0.045–0.3 m is present (Table 1).

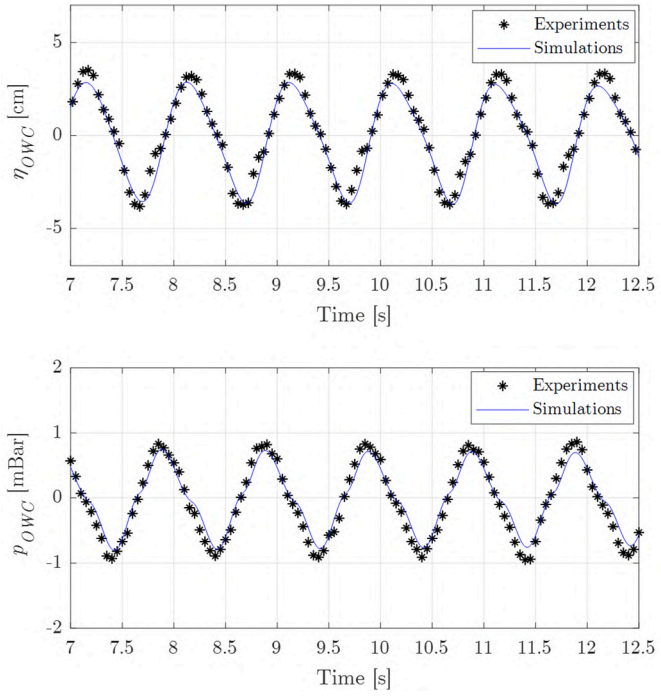

Fig. 3. Comparison between laboratory tests (Simonetti et al., 2017; Crema et al., 2015) and NWT simulations for water level (η_{owc}) and pressure (p_{owc}) in the OWC chamber. Quantities at small scale, for an OWC chamber with draught $D = 0.09$ m, length $W = 0.19$ m, area of the top cover aperture equal to 2% of the top cover area and incident wave with height $H = 4$ cm and period $T = 1$ s.

Regular wave attacks are considered, with height $H = 0.3$–0.8 m and periods T ranging between 3 and 6 s, as characteristic short-wave conditions inside a marina harbour. Numerical simulations are performed in the NWT considering a 1:15 scale model of the device. Geometry and wave conditions are scaled by using Froude similarity.

For a two-dimensional OWC model, the height of the total reflected wave (H_{rr}), the height of the radiated wave (H_{rad}), the height of the water surface oscillation inside the OWC (H_{owc}), the height of the pressure fluctuation inside the chamber (P_{owc}) and the pneumatic power absorbed by the OWC (Π_{owc}) are mainly affected by the following parameters: the incident wave height (H), the incident wave period (T), the water depth (h), the length (W), the draught (D), the top-cover aperture (V) of the OWC chamber, the gravitational acceleration (g), the densities of water and air (ρ_a and ρ_w, respectively) and the air and water dynamic viscosity (μ_a and μ_w, respectively), i.e.:

$$(H_{rr}, H_{rad}, H_{owc}, P_{owc}, \Pi_{owc}) = f(H, T, h, W, D, V, g, \rho_a, \rho_w, \mu_a, \mu_w) \tag{6}$$

Assuming H, T (i.e. equivalently the wavelength L or the wavenumber k via the dispersion relation) and ρ_w as fundamental quantities, the previous expression can be rearranged in terms of dimensionless parameters as follows:

$$\left(K_{rr}, K_{rad}, C_a, C_p, CW\right) = f\left(kh, \frac{W}{L}, \frac{D}{H}, \frac{V}{W}, \frac{gT^2}{H}, \frac{\rho_a}{\rho_w}, \frac{T\mu_a}{\rho_w H^2}, \frac{T\mu_w}{\rho_w H^2}\right) \tag{7}$$

The total reflection coefficient (K_{rr}), the radiation coefficient (K_{rad}), the amplification and pressure coefficients (C_a and C_p) and the capture width ratio CW are defined as:

$$K_{rr} = \frac{H_{rr}}{H} = \frac{H_{rad} + H_r}{H} \tag{8}$$

$$K_{rad} = \frac{H_{rad}}{H} \tag{9}$$

$$C_a = \frac{H_{owc}}{H} \tag{10}$$

$$C_p = \frac{P_{owc}}{\rho_w \cdot g \cdot H} \tag{11}$$

$$CW = \frac{\Pi_{owc}}{\Pi_{wave}} \tag{12}$$

where H_r is the height of the properly reflected component of the total reflected wave field, i.e. excluding the wave radiated by the OWC. Π_{wave} is the incident wave power per unit crest width, computed based on Airy wave theory, as in Eq. (13), being ω the wave frequency.

$$\Pi_{wave} = \frac{1}{16}\rho_w g H^2 \frac{\omega}{k}\left(1 + \frac{2kh}{\sinh(2kh)}\right) \tag{13}$$

Under the hypothesis of incompressible airflow, the mean pneumatic power Π_{owc} [W/m] absorbed per unit width of the OWC chamber is computed from the instantaneous value of air pressure (p_{owc}) and water level (η_{owc}) in the OWC chamber as in Eq. (15)

$$\Pi_{owc} = \frac{1}{T_{test}} \int_0^{T_{test}} p_{owc} \cdot \frac{d\eta_{owc}}{dt} \cdot W dt \tag{14}$$

Concerning the hypothesis of incompressible flow, it is worthwhile to mention that air compressibility is not effective in small scale models of OWC devices which assume full geometric similarity (Weber, 2007;

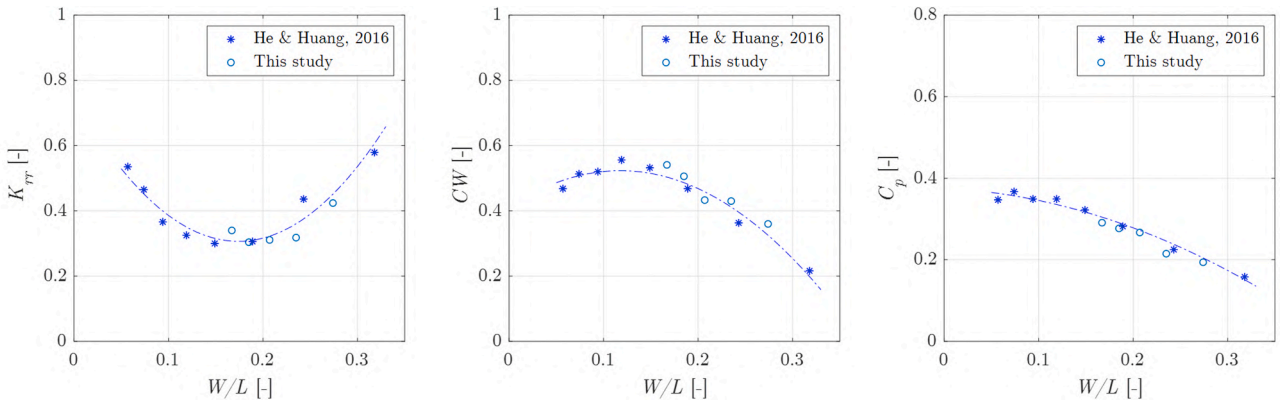

Fig. 4. Comparison between laboratory tests by He and Huang, 2016, and NWT simulations for total reflection coefficient (K_{rr}), capture width ratio (CW) and pressure coefficient (C_p).

Table 1
Test conditions and geometric parameters of the OWC structure. Dimensions at full scale.

Parameter, symbol	Range
Water depth, h	9 m
Range of incident wave height, H	0.3–0.8 m
Range of incident wave period, T	3–6 s
OWC freeboard, Fc	1.5 m
Range of OWC chamber length, W	2–4 m
Range of OWC front wall draught, D	1–2.5 m
Range of top-cover aperture length, V	0.045–0.3 m

Falcão and Henriques, 2014; Simonetti et al., 2018; López et al., 2020). Previous studies (Simonetti et al., 2018) pointed out that neglecting air compressibility when modelling the device may result in a moderate overestimation of the OWC capture width ratio CW (i.e. lower than 10% for the range of parameters of interest in this study).

In this study, ρ_a/ρ_w was kept constant, and the effects of viscosities (of water and air) are considered negligible for the phenomena under study. Moreover, concerning the dimensionless form of gravitational acceleration in Eq. (7), gT^2/H, it can be noted that its numerator is proportional to the deep-water wavelength, i.e. $L_0 = gT^2/(2\pi)$. Therefore, this parameter is inversely proportional to the wave-steepness (H/L_0) and it is strongly correlated to the nonlinear wave regime and its consequences in the physical phenomena. The present work focuses on mild wave-steepness conditions (see Table 2) and wave nonlinearity plays a relatively minor role compared to the other dimensionless parameters. For this reason, the parameter gT^2/H is excluded from the analysis in this study. Based on the generally good collapse of the data shown later in the paper, this assumption seems to be fully confirmed. Under these hypotheses, Eq. (7) can be reduced to:

Table 2
Range of dimensionless parameters in this study.

Parameter, symbol	Range
Range of relative water depth, kh	1.58–3.78
Range of relative OWC chamber length, W/L	0.07–0.23
Range of relative OWC front wall draught, D/H	1.68–4.44
Range of relative top-cover aperture length, V/W	0.025–0.13
Range of dimensionless gravitational acceleration, gT^2/H	$0.11 \cdot 10^3$–$1.17 \cdot 10^3$
Range of dimensionless dynamic viscosity of air, $T\mu_a/\rho_w H^2$	$8.4 \cdot 10^{-8}$ – $1.2 \cdot 10^{-6}$
Range of dimensionless dynamic viscosity of water, $T\mu_w/\rho_w H^2$	$4.7 \cdot 10^{-6}$ – $6.7 \cdot 10^{-5}$
Relative air density, ρ_a/ρ_w	$1.2 \cdot 10^{-3}$
Range of incident wave steepness, H/L	0.007–0.03

$$\left(K_{\mathrm{rr}}, K_{\mathrm{rad}}, C_a, C_p, \mathrm{CW}\right) = f\left(\mathrm{kh}, \frac{W}{L}, \frac{D}{H}, \frac{V}{W}\right) \tag{15}$$

4. Results

Results concerning the reflection properties of the harbour structure embodying the OWC device are analysed using the dimensionless parameter introduced. The effect of the different parameters on the processes inside the device and on its energy harvesting capability is also briefly discussed in this section. Finally, an analysis of the partial-reflection wave field in front of the structure is provided. Original empirical formulae are proposed for the variables having the greatest importance from the harbour engineering practice point of view, namely: (i) the global reflection coefficient K_{rr}; (ii) the ratio of the height of the pseudo-antinode of the partial-reflection wave filed in front of the structure to the incident wave height H_v/H.

4.1. Total reflection coefficient K_{rr}

The total reflection coefficient K_{rr} obtained for the tested wave conditions and geometries varies in the range 0.15–0.9. The relative chamber length W/L has a dominant impact on K_{rr}, i.e. on the value of the overall wave reflection plus radiation from the OWC chamber, and on the phase difference of these two components (i.e. destructive or constructive interference, as discussed in Cappietti and Simonetti (2018)). Minimum values of K_{rr} are obtained for relative chamber length W/L around 0.1–0.17 (Fig. 5). The highest K_{rr} values are found for W/L = 0.07–0.09 and relative water depth $kh = 1.58$. For the same structure length W/L, a lower K_{rr} (~0.4–0.5) is obtained for higher kh values. Indeed, for a given W/L value, relatively large variations in K_{rr} occur when varying the relative water depth kh or the other design parameters of the OWC. Different trends of K_{rr} vs D/H are observed for different relative water depth kh. For $kh = 3.78$, $V/W = 0.1$ and $W/L = 0.2$, K_{rr} decreases from around 0.6 to 0.45 and 0.25 as D/H decreases from 3.3 to 2.5 and 1.7, respectively (Figs. 5 and 6). Instead, for $kh = 2.31$, V/W = 0.1 and $W/L = 0.12$, K_{rr} at first decreases with increasing D/H (from 0.4 for D/H = 1.7 to 0.16 for D/H = 3.3), then it increases with further increase of D/H (up to $K_{rr} = 0.3$ for $D/H = 3.8$, Fig. 6). The increase of K_{rr} beyond a threshold value of D/H (which is, in turn, a function of the structure geometry and the relative water depth kh) may be due to the increased blockage effect of the front wall of the OWC, which directly reflects a greater fraction of the incident wave energy. The relevant effect of both D/H and kh on K_{rr} is a consequence of the OWC basic working principle: the total reflection results from a balance between the fraction of energy converted into pneumatic energy, dissipated for friction effects or involved in vortex shedding and that reflected by the front and back walls of the structure. The energy converted into

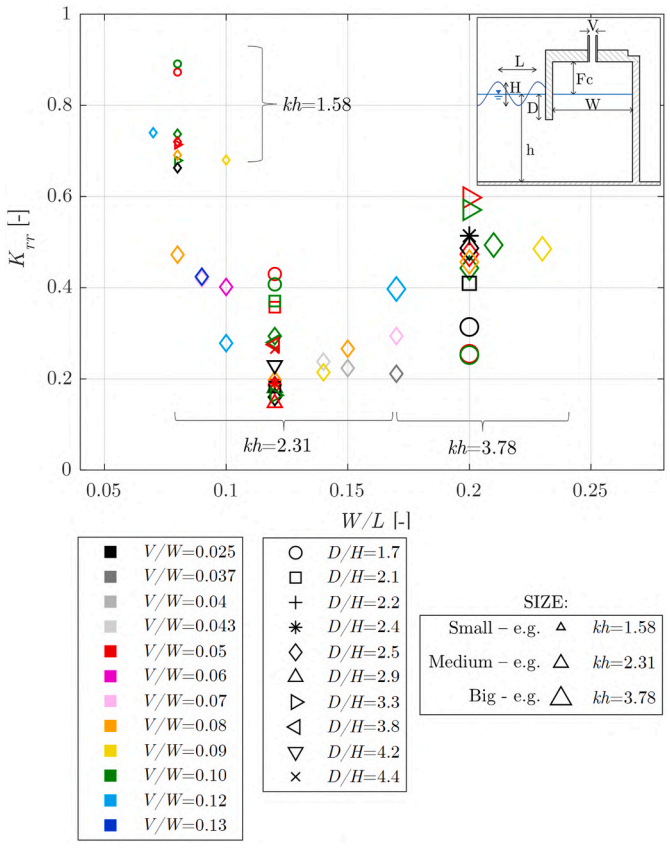

Fig. 5. Variation of total reflection coefficient (K_{rr}) versus relative chamber length W/L.

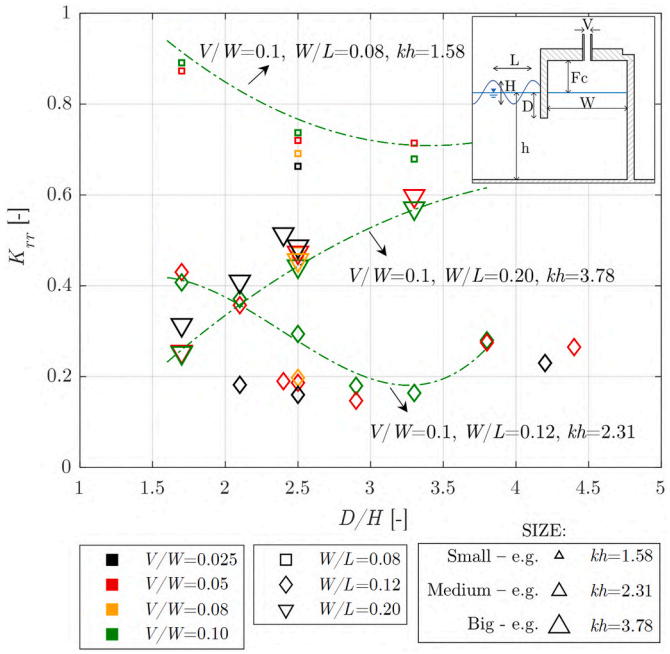

Fig. 6. Variation of total reflection coefficient (K_{rr}) versus relative front wall draught D/H. For the sake of readability, results are shown only for $W/L = 0.08$, $W/L = 0.12$ and $W/L = 0.20$.

pneumatic form is directly related to the OWC resonant frequency, which is in turn primarily determined by the front wall draught D (Evans and Porter, 1995; McCormick, 2007). Varying kh, i.e. changing the incident wave period for a given water depth h, results in a shift of the working conditions with respect to resonance, thus changing the fraction of energy converted into pneumatic form. The energy reflected by the front wall is also strongly influenced by the depth of the front wall itself, i.e. D (in the limit case of $D > L/2$, the OWC would behave as a vertical wall as far as wave reflection is concerned).

The top-cover aperture size V/W has a lower impact on K_{rr} respect to the other parameters (Fig. 7). It can be observed, by way of example, that for relative water depth $kh = 1.58$, $W/L = 0.08$ and $D/H = 2.5$, K_{rr} increases from 0.66 to 0.74 when V/W increases from 0.025 to 0.10. For $kh = 2.31$, $W/L = 0.12$ and $D/H = 2.5$, a similar trend of increase is observed (with K_{rr} varying from 0.16 to 0.29). For the same D/H and $W/L = 0.20$, no remarkable effect of V/W on K_{rr} is observed, instead, for $kh = 3.78$ (with K_{rr} varying less than 4 percentage points for the same variation of V/W).

4.1.1. Prediction formula for K_{rr}

Based on the available dataset, an empirical formula relating the fundamental dimensionless parameters in Eq. (15) (kh, W/L, D/H and V/W) to K_{rr} is proposed (Fig. 8 and Table 3). A dimensionless parameter Γ, defined in the form of a power product as in Eq. (16), accounts for the combined effect of the aforementioned fundamental parameters.

$$\Gamma = (W/L)^{\alpha} \cdot (D/H)^{\beta} \cdot (V/W)^{\gamma} \cdot (kh)^{\delta} \tag{16}$$

The functional relation f_1 between Γ and K_{rr} is imposed in the form of a rational polynomial as in Eq. (17). The numerical coefficients of f_1, together with the exponents α, β, δ, γ in the power product Γ, are determined based on a non-linear regression aimed at maximizing the determination coefficient R^2 and minimizing the *Root Mean Square Error* (RMSE) of the fit between the predictions of the formula and the available data (as summarized in Table 3).

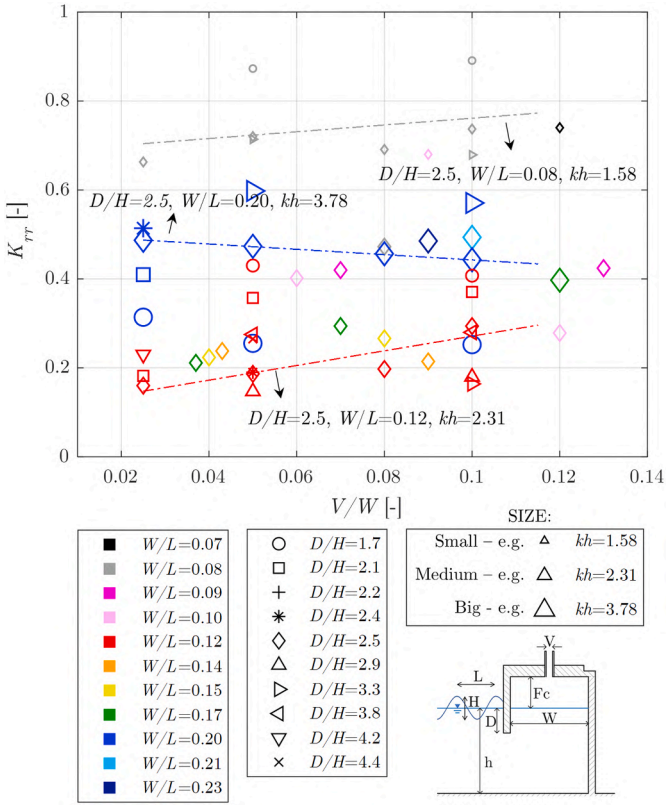

Fig. 7. Variation of total reflection coefficient (K_{rr}) versus relative top-cover aperture V/W.

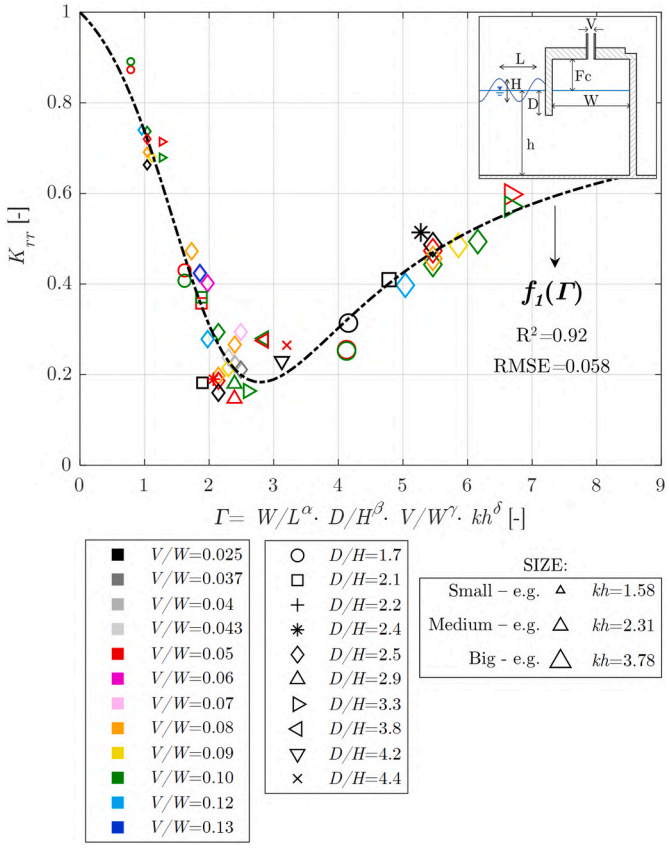

Fig. 8. Fit between total reflection coefficient (K_{rr}) from numerical simulations and predictions of the empirical formula f_1 (Γ) (dotted line).

Table 3
Empirical formula for the prediction of the global reflection coefficient K_{rr} with values of numerical coefficients.

$\Gamma = (W/L)^{\alpha} \cdot (D/H)^{\beta} \cdot (V/W)^{\gamma} \cdot (kh)^{\delta}$	$\alpha = 0.5$	$\beta = 0.7$	$\gamma = 0$	$\delta = 1.4$
$K_{rr} = f_1(\Gamma) = \frac{p_1\Gamma^2 + p_2\Gamma + p_3}{\Gamma^2 + q_1\Gamma + p_3}$	p_1 = 0.86	p_2 = −4.45	p_3 = 6.5	q_1 = −3.55

$$f_1(\Gamma) = \frac{p_1\Gamma^2 + p_2\Gamma + p_3}{\Gamma^2 + q_1\Gamma + p_3} \quad (17)$$

The proposed formula is to be considered valid in the range of parameters studied in this work: W/L = 0.07–0.23, D/H = 1.68–4.44, V/W = 0.025–0.13, kh = 1.58–3.78. The formula shows a strong correlation with the available K_{rr} data (determination coefficient R^2~0.9, with RMSE = 0.058, Fig. 8). Values of K_{rr} lower than 0.3 are obtained for $2 < \Gamma < 4$. The higher observed K_{rr} values (0.9–0.7) correspond to $\Gamma < 1$.

4.2. Radiation coefficient K_{rad}

The amplitude of the wave radiated by the OWC and the resulting radiation coefficient K_{rad} (defined as in Eq. (9)) is fundamentally determined by the amplitude of the pressure fluctuation inside the OWC air chamber, expressed in terms of dimensionless pressure coefficient C_p (Eq. (11)). For values of the dimensionless pressure coefficient C_p varying from 0 to 0.33, K_{rad} varies between 0 and 0.40 (Fig. 9). Similar shapes of the functional dependence of K_{rad} on C_p are observed for different relative water depth kh, but the rate of increase of K_{rad} with C_p is different: for the same C_p, higher values of K_{rad} are found for the intermediate kh = 2.31, while lower values are obtained with both kh = 1.58 and kh = 3.78. Therefore, a value of kh (i.e. of the incident wave period for a fixed water depth h) maximizing wave radiation exists, as expected from prediction models based on linear wave theory (Sarmento and Falcão, 1985; Brendmo et al., 1996; Martins-Rivas and Mei, 2009; Mei, 2012). It is worthwhile noting that K_{rad} also depends on the relative chamber length W/L, as explicitly shown in Fig. 10. However, the functional dependence of K_{rad} on C_p is primarily driven by kh. Indeed, for a given kh, the same functional dependence of K_{rad} on C_p can be assumed for different values of W/L (Fig. 9). For fixed relative front wall draught D/H = 2.5 and kh = 2.31, the higher radiation coefficients K_{rad} are found for relative chamber length W/L = 0.12–0.16 (Fig. 10). For such configurations, varying W/L between 0.08 and 0.17 results in a variation of K_{rad} of the order of 5 percentage points, confirming the lower importance of the parameter W/L respect to kh. Further, regardless of the value of V/W, the dependence of K_{rad} on W/L has a similar shape, but with a different maximum value, for different values of the top-cover aperture size V: indeed, the damping applied to the OWC chamber, i.e. the relation between the air pressure and the resulting airflow through the aperture, is a function of V only (as shown e.g. in Simonetti et al., 2017). For higher damping, i.e. smaller V, the maximum K_{rad} is lower than for smaller applied damping.

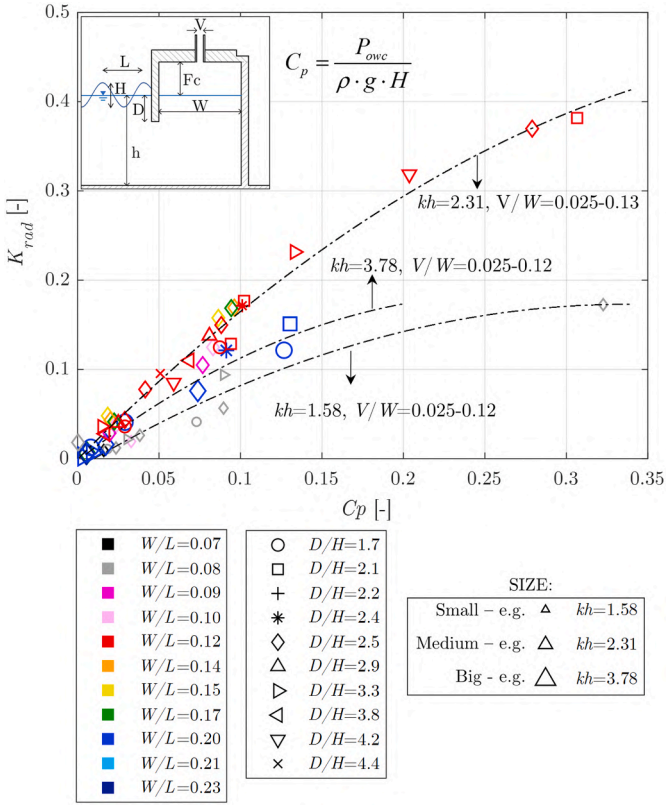

Fig. 9. Variation of radiation coefficient (K_{rad}) versus dimensionless pressure coefficient C_p.

Among the OWC structure parameters, the relative top-cover aperture V/W has a paramount impact on the radiation coefficient K_{rad} (Fig. 11). The rate of decrease of K_{rad} with V/W is exponential, with different decay constants for different kh and W/L. For high values of V/W (>0.1), i.e. big apertures on the OWC top-cover, the outgoing radiated waves are small (K_{rad}<0.05) regardless of the other OWC parameters and wave conditions. This is a direct consequence of the lower pressure oscillation inside the air chamber P_{owc} for higher V/W (later discussed in *section 4.3*, Fig. 15). For the limit case of V/W = 0 (i.e. a chamber completely open to the atmosphere), there would be no dynamic air pressure oscillation on the free surface, resulting in null wave radiation towards the exterior. For the lowest tested values V/W=0.025, K_{rad}

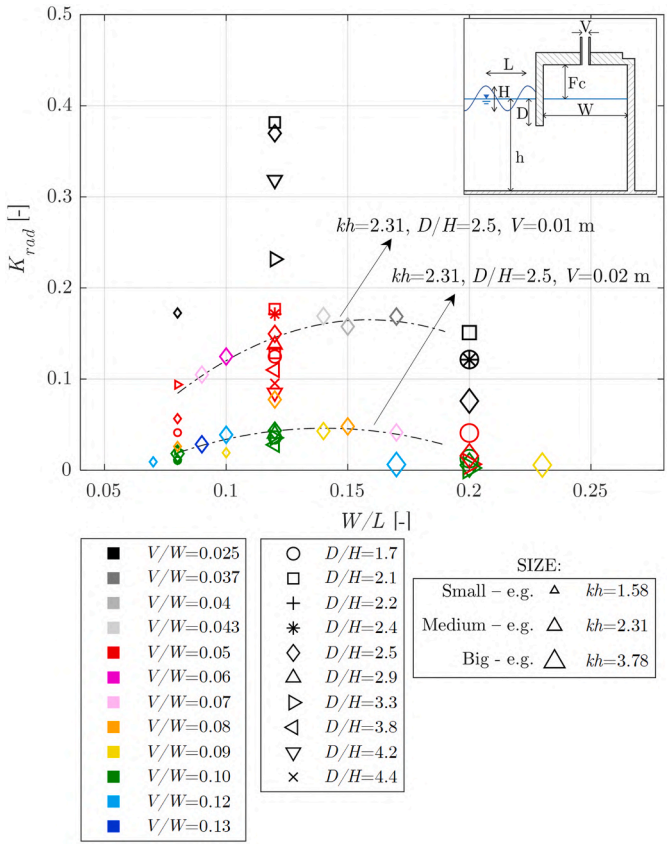

Fig. 10. Variation of radiation coefficient (K_{rad}) versus relative chamber length W/L.

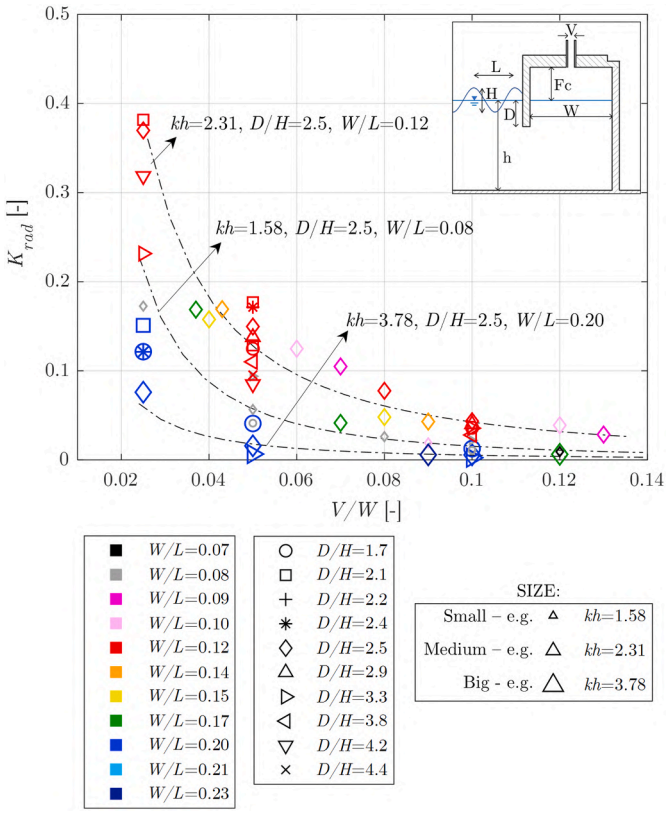

Fig. 11. Variation of radiation coefficient (K_{rad}) versus relative top-cover aperture V/W.

varies from around 0.05 (for kh = 3.78, D/H=2.5 and W/L = 0.2) to around 0.4 (for kh = 2.31, D/H=2.5 and W/L = 0.12).

The relative front wall draught D/H also influences K_{rad}, although in a more limited way than V/W. In the range of tested conditions, varying D/H results in a maximum variation of K_{rad} lower than 10 percentage points (Fig. 12). As previously observed for K_{rr} (*section 4.1*), different trends of K_{rad} with D/H are found for different relative water depth kh. For kh = 2.31 and 3.78, K_{rad} decreases when D/H increases from 1.7 to 4.4. On the contrary, for the lowest kh = 1.58, K_{rad} tends to increase with D/H (e.g. for the configuration V/W = 0.05 and W/L = 0.08 in Fig. 12). This effect may be due to the shift in the OWC resonant frequency determined by different D: higher values of D corresponds to a lower resonant frequency of the chamber (McCormick, 2007). For longer incident waves (i.e. lower kh-values for fixed h) increasing values of D (i.e. increasing D/H for fixed H) will cause the device to work closer to resonance. Approaching resonance conditions implies, in turn, an increase in the OWC capture width ratio CW, which determines an increase in the radiation coefficient K_{rad} (as underlined in *section 4.3*, Fig. 17). Such a hypothesis can be verified by determining the resonance frequency of the OWC with simple analytical formulations, as exemplary done in Appendix B for the cases here discussed.

Both destructive and constructive interference phenomena between the radiated and the reflected wave fields are observed for the simulated OWC geometries. The ratio of the radiated wave height H_{rad} to the total reflected wave height (H_{rr}), which results from the sum of the properly reflected and the radiated waves (Eq. (9)), reaches a maximum of H_{rad}/H_{rr}=*2.5* for the OWC configuration having W/L = 0.12, V/W = 0.025 and D/H = 2.5, with kh = 2.31 (Fig. 13). Values of $H_{rad}/H_{rr} > 1$ denote the occurrence of destructive interference between the properly reflected and the radiated wave fields. Such a phenomenon is remarkably influenced by the relative chamber length W/L and by the relative top-cover aperture V/W. Within the tested configurations, values of H_{rad}/H_{rr} > 1 are found for W/L = 0.12 and V/W < 0.05 (Fig. 13). For increasing V/W, H_{rad}/H_{rr} tends to zero, due to the progressive decrease of the height of the radiated wave field induced by the decreasing pressure oscillation inside the OWC for bigger apertures in the top cover.

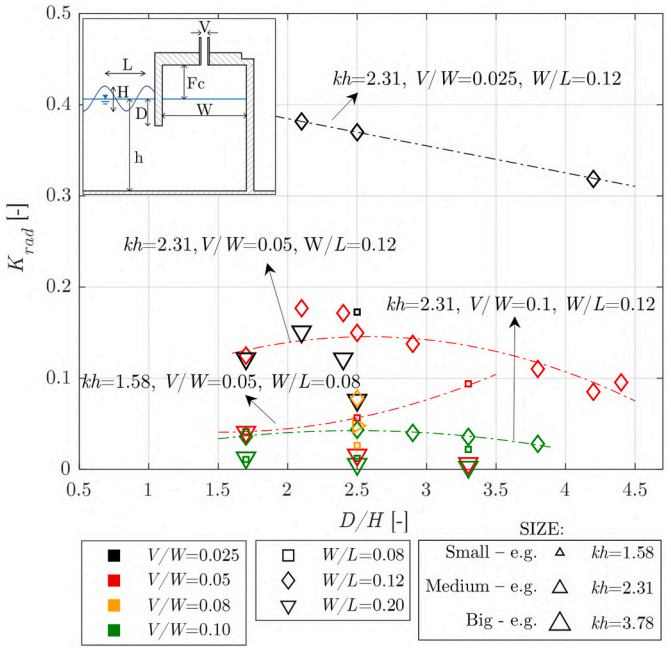

Fig. 12. Variation of radiation coefficient (K_{rad}) versus D/H. For the sake of readability, results are shown only for W/L = 0.08, W/L = 0.12 and W/L = 0.20.

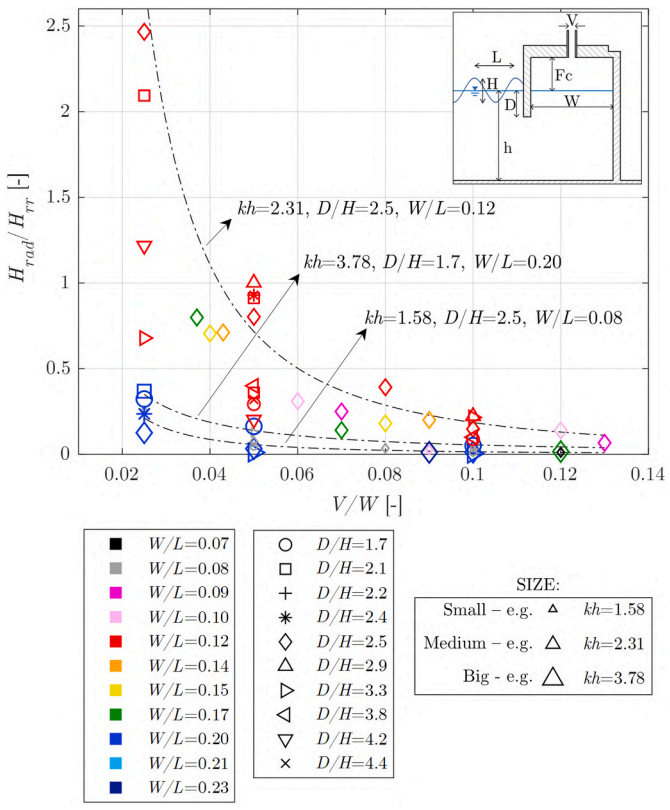

Fig. 13. Variation of the ratio of radiated wave height to radiated plus reflected wave height H_{rad}/H_{rr} versus V/W.

4.3. Processes inside the OWC structure and hydrodynamic performance

An in-depth discussion of the effect of geometry parameters and wave conditions on the performance of OWC structures as wave energy converters is out of the scope of the present work. Several specific previous studies are available in the literature on such topic (Ning et al., 2016; He et al., 2016; Simonetti et al., 2017; Elhanafi et al., 2017a; López et al., 2019; Zabihi et al., 2019). In this section, only those aspects related to the processes inside the OWC which are more relevant to support the discussion of its performance as an anti-reflection device are highlighted.

The relative height of the free surface oscillation inside the OWC chamber, expressed in terms of amplification factor C_a (Eq. (10)), is primarily influenced by the value of the relative chamber length W/L (Fig. 14, a) and varies between approximately 0.5 (for $W/L > 0.20$) and 2.5 (for $W/L < 0.08$). The other OWC parameters, namely D/H and V/W, also influence C_a. Within the whole range of parameters considered (Table 2), for fixed W/L and kh and varying D/H and V/W, C_a varies from 1.8 to 2.5 for $W/L = 0.08$ ($kh = 1.58$), from 1.4 to 2 for $W/L = 0.12$ ($kh = 2.31$) and from 0.4 to 0.9 for $W/L = 0.2$ ($kh = 3.78$). Fixing kh and

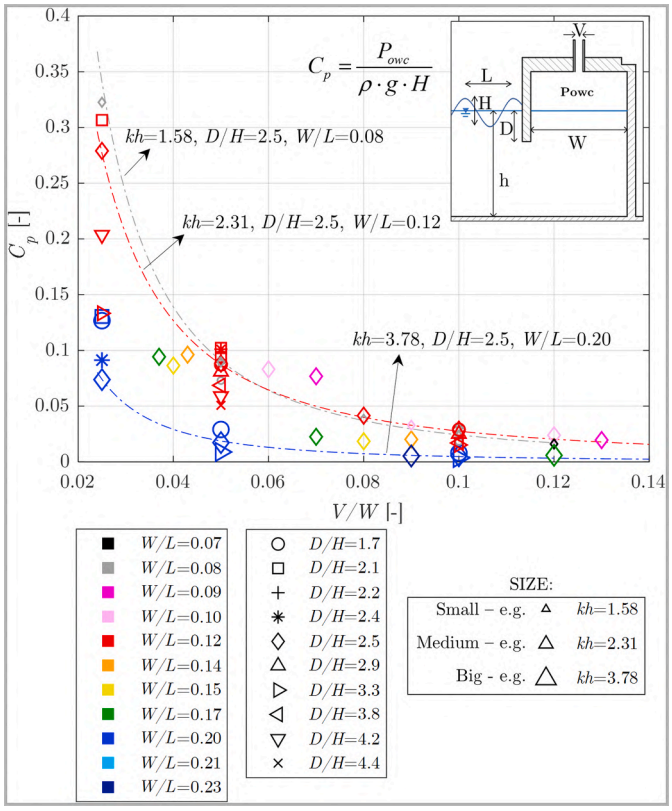

Fig. 15. Variation pressure coefficient Cp versus V/W.

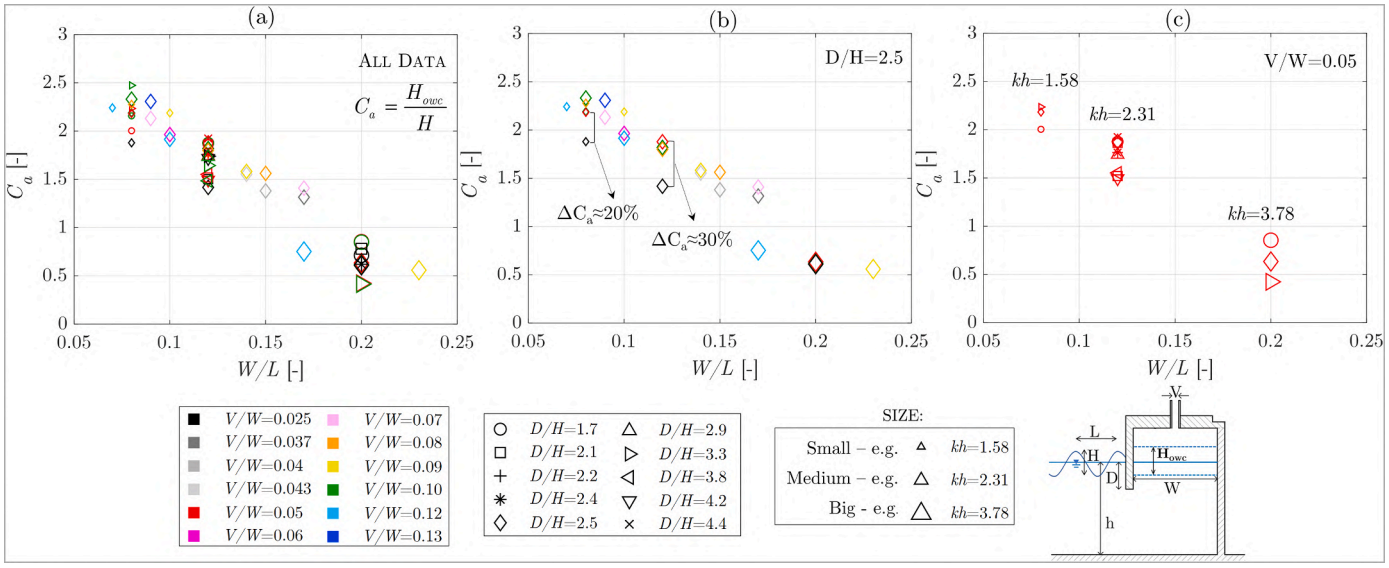

Fig. 14. Variation of the OWC absorption coefficient Ca versus W/L for the whole dataset (a), cases with D/H = 2.5 only (b) and cases V/W = 0.05 only (c).

D/H, doubling the value of V/W results in relative variations of C_a up to 30% (as exemplarily shown in Fig. 14, b, where only the results for $D/H = 2.5$ are shown for aiding the readability of the figure). For $kh = 3.78$ and $V/W = 0.0.5$ (Fig. 14, c), C_a progressively increases from 0.4 to 0.6 and 0.85 when D/H decreases from 3.3 to 2.5 and 1.7, respectively, while the opposite trend can be observed for $kh = 1.58$. A non-monotonic trend of C_a with D/H is observed for $kh = 2.31$, with higher values for $D/H = 2.4$. The pressure coefficient C_p, instead, is mainly influenced by V/W (Fig. 15). C_p decreases with increasing V/W, i.e. increasing the size of the top-cover aperture relative to the structure length, as expected. For $V/W > 0.1$, C_p tends to converge to low values (<0.03) despite the value of D/H, W/L and kh.

As a result of the combined effect of air pressure and water level variation in the chamber, as expressed by Eq. (14), for the OWC geometries studied in this work, increasing values of the OWC capture width ratio CW are found when decreasing the relative orifice aperture V/W (Fig. 16). A maximum value of CW of around 0.49 is obtained for $kh = 2.31$, W/L=0.12, $V/W = 0.025$ and $D/H = 2.1$, with a corresponding value of the total reflection coefficient $K_{rr} = 0.18$. It is worth to stress that the trend of CW with V/W, substantially monotonic in the range of parameters of interest in this study, is not expected to be monotonic in general, as widely proved in previous studies. Indeed, for a give chamber length and draught, an optimal value of the orifice aperture V exists (Ning et al., 2016; Simonetti et al., 2017; Elhanafi et al., 2017a; Sarmento, 1993; Sheng et al., 2012; Lopez et al., 2014), and further decreasing it would result in a lower CW. An approximately linear relation is found between the value of CW and the radiation coefficient K_{rad} (Fig. 17), which directly reflects the dependence of both the quantities on the air pressure inside the OWC chamber. The angular coefficient of the linear correlation varies with kh: for a given K_{rad}, higher CW values are obtained for the smaller $kh = 1.58$ (i.e. longer incident waves). It is expected that greater values of CW can be obtained by adapting the geometry parameters of the OWC, as discussed e.g. by Elhanafi et al. (2016a) and Simonetti et al. (2017), while maintaining a satisfactory performance of the device in terms of reflection coefficients.

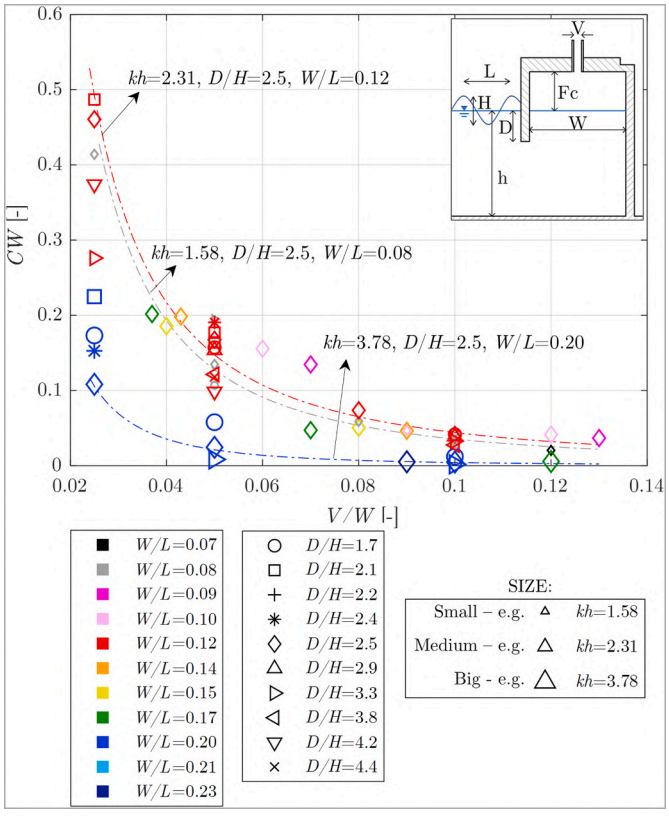

Fig. 16. Variation of the OWC capture width ratio CW versus V/W.

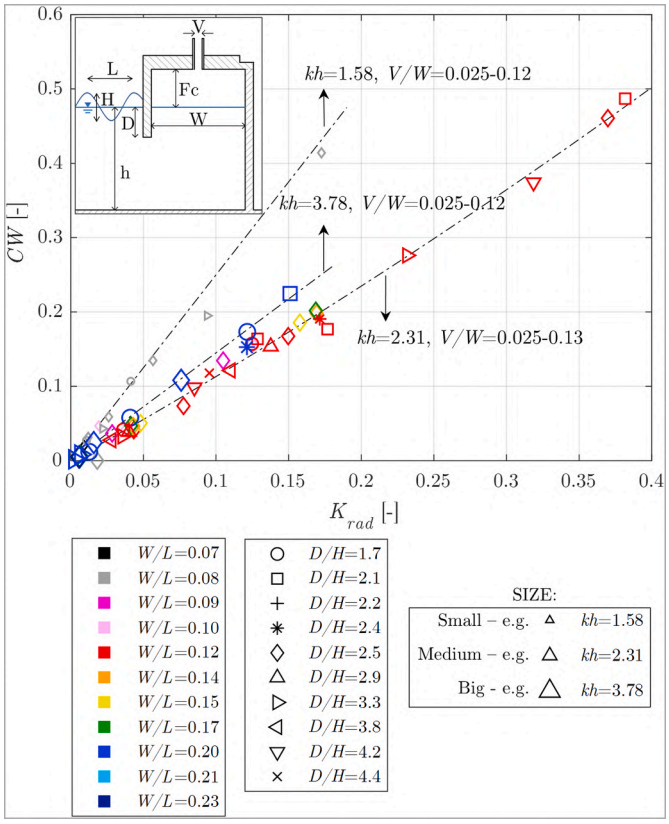

Fig. 17. Variation of the OWC capture width ratio CW versus K_{rad}.

4.4. The wave field in front of the structure embodying the OWC

The global agitation in front of the structure is quantified by analysing the envelope of the wavefield obtained from the 3rd step simulations in the NWT, with the methodology described in *section 2.2*. The wave field in front of the breakwater englobing the OWC structure is characterized by the superposition of the incident wave, the properly reflected wave and the wave produced by the pulsating air pressure inside the OWC chamber, which propagates towards the exterior (i.e. the radiated wave). Unlike the case of reflection from a vertical wall, the wave reflection from a breakwater embodying an OWC is partial, since part of the energy is either absorbed by the device or dissipated by real fluid effects. Therefore, the resulting wave field is a quasi-standing wave field, in which quasi-antinodes (with height H_v) and quasi-nodes (with height H_n) are present (Fig. 18). The characteristic of the quasi-standing field depends on the entity of the properly reflected and the radiated waves, and on the phase difference between the incident and the reflected plus radiated wave trains, which are, in turn, a function of the geometric parameters of the OWC structure and of the incident wave characteristics.

The value of the total reflection coefficient K_{rr} can be also obtained from the analysis of the envelope of the partial standing wave field for imperfect reflection of monochromatic, linear waves as (Healy, 1951):

$$K_{rr} = \frac{H_v - H_n}{H_v + H_n} \tag{18}$$

Comparing the estimation of K_{rr} obtained with direct measurements in the previous sections (1st step simulations in Fig. 2) to that based on the envelope analysis as in Eq. (18), a satisfactory agreement is found, with $R^2 = 0.92$ and RMSE equal to 0.053 (Fig. 19).

The ratio of the quasi-antinode height H_v to the far-field incident

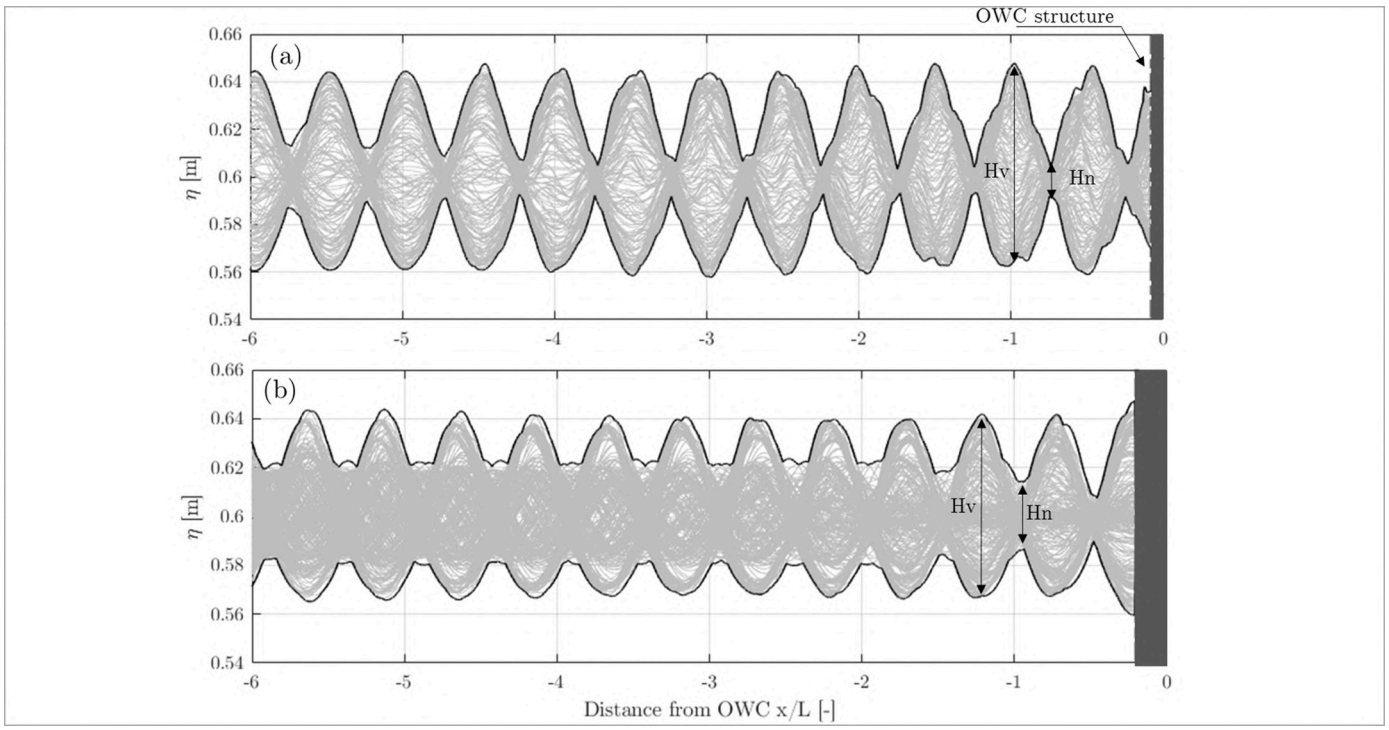

Fig. 18. Envelope of the quasi standing wave field in front of the OWC (H_v: quasi-antinode height, H_n: quasi-node height) for configurations $W/L = 0.07$, $D/H = 2.4$, $V/W = 0.12$, $kh = 1.58$ (a) and $W/L = 0.2$, $D/H = 3.2$, $V/W = 0.05$, $kh = 3.78$ (b). Results for $H/h = 0.067$ m, $h = 0.6$ m.

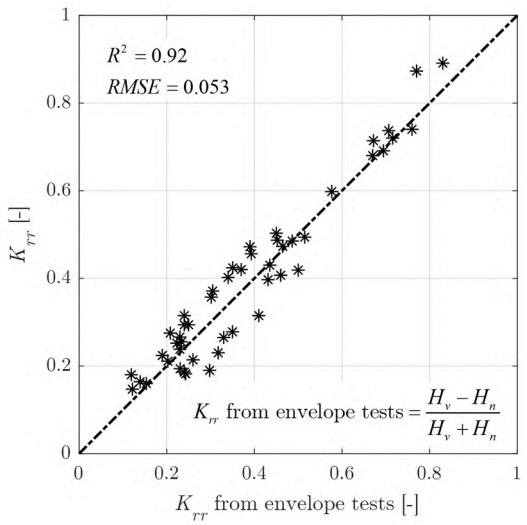

Fig. 19. Scatter plot of direct estimations of K_{rr} versus K_{rr} estimated from the analysis of the envelope of the wave field in front of the structure.

wave height H approaching the structure, H_v/H, provides a direct indication of the total agitation of the wave field and could be relevant for practical design purpose of such kind of structure. For this reason, a prediction formula for H_v/H is provided as follows.

4.4.1. Prediction formula for H_v/H

The same dimensionless parameter Γ expressing the dependence of K_{rr} on the fundamental parameters (defined as in Eq. (16) and Table 3) is used here. The functional relation f_2 between Γ and H_v/H is imposed in the form of the rational polynomial in Eq. (19). The numerical coefficients of f_2 (summarized in Table 4) are determined based on nonlinear regression.

Table 4
Empirical formula for the prediction the ratio of the quasi-antinode height to the far-field incident wave height, H_v/H, with values of numerical coefficients.

$\Gamma = (W/L)^{\alpha}\cdot(D/H)^{\beta}\cdot(V/W)^{\gamma}\cdot(kh)^{\delta}$	$\alpha = 0.5$	$\beta = 0.7$	$\gamma = 0$	$\delta = 1.4$
$\frac{H_v}{H} = f_2(\Gamma) = p_4\Gamma^2 + p_5\Gamma + 2p_6/\Gamma^2 + q_2\Gamma + p_6$	$p_4 = 2.22$	$p_5 = -12.9$	$p_6 = 12$	$q_2 = -5.45$

$$f_2(\Gamma) = p_4\Gamma^2 + p_5\Gamma + 2p_6/\Gamma^2 + q_2\Gamma + p_6 \quad (19)$$

Also in this case, the proposed formula should be used only within the range of parameters considered in this work (summarized in Table 2). The formula has $R^2 = 0.87$ and RMSE = 0.091 with the available data (Fig. 20).

For the range of OWC geometries and wave conditions of this study, H_v/H varies between 1.93 (i.e. the wave field in front of the structure is similar to that in front of a vertical wall) and 1.1. Values of H_v/H lower than 1.4 are found for $2 < \Gamma < 4.4$.

5. Discussion

Values of the total reflection coefficient K_{rr} obtained for the vertical breakwater embodying the OWC structure vary between around 0.15 and 0.9. For the same type of structure, minimum values of K_{rr} around 0.2 (for relative chamber length $W/L = 0.12$) were also obtained, for regular waves, in the large scale laboratory tests by Viviano et al., 2016, 2019.

The parameter W/L is used to perform a comparison between reflection coefficients K_{rr} of the OWC and those of other low-reflectivity structures, since it is a direct index of the space required to construct the structure. Comparing the results in this study to those from selected datasets available in the literature for caissons with a frontal perforated wall (Fig. 21, a), for relatively small W/L similar values of K_{rr} are found

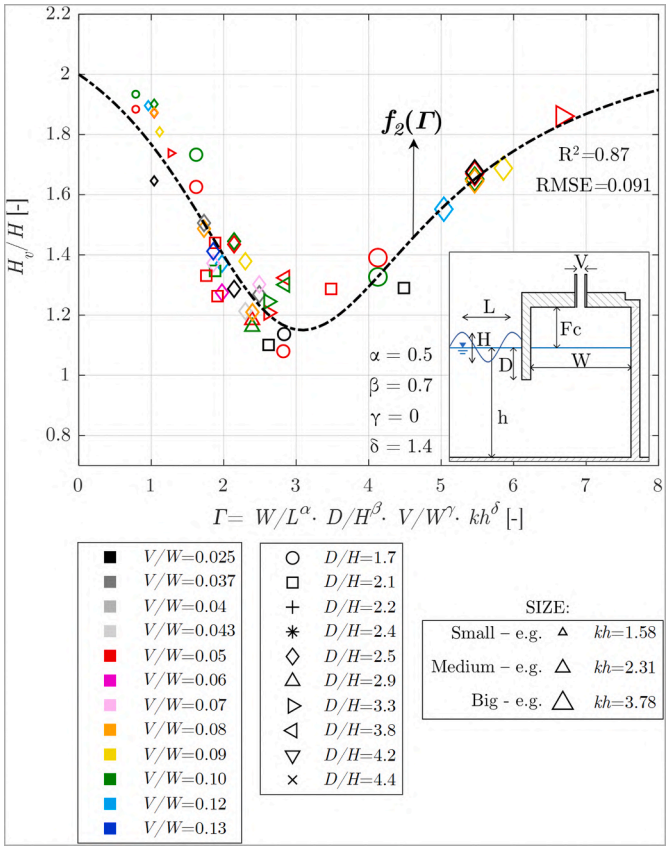

Fig. 20. Fit between the ratio of the quasi-antinode height to the far-field incident wave height, H_v/H, and the predictions of the empirical formula $f_2(\Gamma)$ (dotted line).

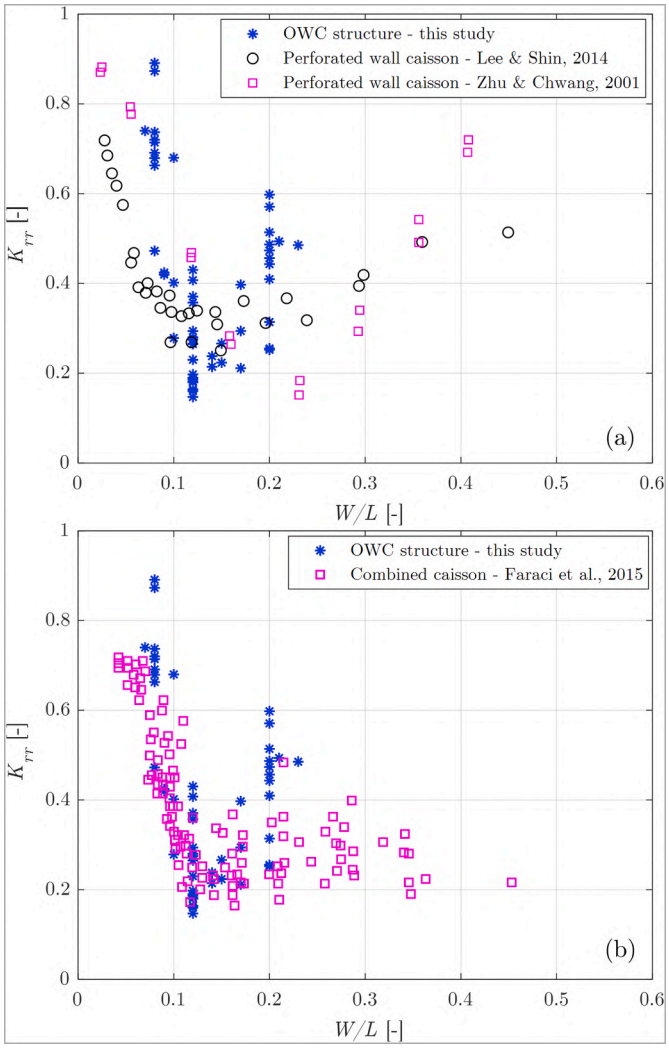

Fig. 21. Comparison between total reflection coefficient K_{rr} for the OWC structure in this study and that of caissons with frontal perforated wall tested by Lee and Shin, 2014 (for the single-chamber case with porosity 20%) and Zhu and Chwang, 2001 (for porosity 20% and immersed depth of the perforated wall of $D/h = 1$ and $D/h = 0.5$ (a) and that of combined caissons (perforated seawall plus internal rubble mound) tested by Faraci et al., 2015 (b).

for the two types of structure, with K_{rr} = 0.7–0.9 for W/L = 0.05–0.08. The minimum K_{rr} is similar (around 0.15) for the OWC and the perforated wall caisson tested by Zhu and Chwang (2001). The minimum K_{rr} is obtained for W/L = 0.12 for the OWC and W/L = 0.25 for the perforated caisson. Slightly higher minimum values of K_{rr} (around 0.3) were reported in the dataset by Lee and Shin (2014). For $W/L > 0.2$, the performance of the OWC structure in terms of wave energy reflection decreases (with K_{rr} values of 0.5–0.6). The same trend is observed for perforated wall caissons, even if for such structures lower reflection coefficients are found over a wider range of W/L (denoting better performance in absorbing relatively short waves compared to the chamber length).

The OWC also shows minimum K_{rr} values analogous to those of the combined caisson tested by Faraci et al. (2015) (i.e. caisson with a perforated frontal wall and an internal rubble mound). Indeed, the wave energy reflection performance of the two structures follows similar trends for $W/L > 0.2$ (Fig. 21, b). However, the combined caisson seems to be able to maintain lower values of K_{rr} (<0.4) also in the range $0.2 < W/L < 0.5$.

It is worth noting that in the case of single-chamber perforated caissons, minimum values of the reflection coefficient are generally obtained when the relative length of the structure W/L is 0.25, due to destructive interference phenomena (Fugazza and Natale, 1992; Zhu and Chwang, 2001). For W/L = 0.25 the perforated wall of the caisson stands approximately at a node of a standing wave pattern. For the OWC structure in this work, instead, minimum K_{rr} values are obtained for lower relative length of the caisson (W/L = 0.1–0.15, Fig. 5). The same trend towards a decrease of the optimal W/L value was observed for combined caisson (Faraci et al., 2015) and multiple slotted-walls structures (Lee and Shin, 2014; Neelamani et al., 2017) (Fig. 21). This can be explained by an increase of inertial resistance which causes a phase difference between the inside and the outside of the chamber, moving the position of the node closer to the back wall of the structure (a similar explanation is also given by Faraci et al., 2015). The inertial resistance is due to the inner rouble-mound structure for combined caisson and to the presence of the porous inner walls in perforated-wall structures. For the OWC, such an effect may be related, from one side, to the damping applied on the chamber by the presence of the top-cover aperture and, from the other side, to the consequent phase difference between the radiated and the reflected wave.

In this study, the performance of the structure is analysed only under regular waves. This is mainly due to the use of numerical modelling and the need to maintain a feasible computational time. In turn, numerical modelling was required to study separately the total reflected and the properly radiated wave fields, as discussed in *section 2.2*. For low-reflective quay walls with an internal rubble mound, Altomare and Gironella (2014) found that the range of variation of reflection coefficients was approximately the same in regular and irregular wave tests. Also for combined caissons, similar values of reflection coefficients were found for regular and irregular waves (Faraci et al., 2015). However, differences in reflection coefficients in irregular waves for the specific case of a vertical wall harbour structure embodying an OWC

should be evaluated in future research. As aforementioned, mild wave-steepness conditions are considered. A further extension of the present work could also include the evaluation of the effect of highly nonlinear waves on the anti-refection performance of the structure.

Moreover, in this study, an aperture on the top cover of the OWC structure is present. Up to date, this is the standard laboratory procedure for reproducing the interaction between the air turbine eventually equipping the device and the hydraulic caisson. This approach was used since the first tests by Robinson and Murray (1981) to the most recent ones by López et al. (2020). If a real turbine was used to equip the OWC structure for power-take-off, the resulting interaction between the reflected and the radiated wave components could be altered respect to the simple top-cover aperture case, especially in terms of phase difference between wave components. Such an effect should be assessed in-depth in future research incorporating a high-fidelity model of the turbine as well. This aspect is out of the scope of the present work, which is mainly focused on the OWC structure as a wave energy attenuator rather than a wave energy converter. The considered hydraulic structure is not necessarily to be equipped with an air turbine for wave energy harvesting, which is only regarded as a secondary aspect in this framework.

6. Conclusions

This work investigates the possibility of using OWC structures to reduce the agitation in front of vertical wall harbour structures. The focus of the work is on the total wave reflection (i.e. the sum of properly reflected waves and waves radiated towards the exterior by the OWC) and the interaction between reflected and radiated fields. Water depth and wave conditions have been chosen to represent a relatively low-energy environment that might characterize a harbour area. The performance of such structures concerning wave energy reflection is investigated via numerical modelling (based on computational fluid dynamics), validated with laboratory tests results.

The radiated and properly reflected wave components are explicitly decomposed by performing numerical simulations in which the time series of air pressure inside the OWC chamber is imposed as a boundary condition and the height of the wave radiated outside the OWC structure is directly measured. The interference between the properly reflected wave and that radiated by the OWC can be destructive or constructive. Due to the phenomenon of destructive interference, the total reflected wave height H_{rr} can be lower than the properly reflected (H_r) or the radiated (H_{rad}) wave heights alone.

Minimum values of the total reflection coefficient K_{rr} of around 0.15 are found, therefore the OWC device could be effectively used to reduce wave reflection at vertical wall harbour structures. The minimum K_{rr} is, indeed, similar to that obtained for more-consolidated low-reflectivity structures, i.e. caisson with a perforated seawall or combined caisson. However, the performance of perforated and combined caisson in terms of wave reflection seems to be slightly better for high values of the relative chamber length W/L, i.e. for reducing the reflection of shorter waves. On the other hand, compared to more consolidated wave absorbing structures, the use of OWC devices would allow harvesting the wave energy into a useable form, rather than just dissipating it.

Within the tested conditions, when K_{rr} is at its minimum, the OWC has a value of the capture width ratio CW of around 0.50. By optimizing the geometry parameters of the device, the wave energy extraction performance could further be improved.

From the analysis of the effect of the OWC structure parameters and the hydrodynamic conditions on the reflection properties of the structure, the following main conclusions can be drawn:

(i) The total reflection coefficient K_{rr} is primarily influenced by the relative camber length W/L, with minimum values for W/L = 0.1–0.17. The relative draught D/H and water depth kh, which are determinant on the OWC resonant frequency and its functioning as a wave energy absorber, also relevantly affect K_{rr}.

(ii) The wave radiated by the OWC structure is mainly determined by the amplitude of the pressure fluctuation inside the OWC chamber, expressed in terms of pressure coefficient C_p, with increasing radiated wave heights H_{rad} for increasing C_p. The value of C_p is, in turn, fundamentally determined by the size of the aperture on the top-cover of the OWC. The interaction of the radiated and the reflected wave fields, i.e. the way the phase of these components sum up to determine constructive or destructive interference, is instead mainly related to other structural parameters, e.g. the relative OWC chamber length W/L. For the OWC geometries tested in this work, significant destructive interference phenomena occur between the radiated and the properly reflected waves, with the radiated component alone up to 2.5 times higher than the total reflected wave.

(iii) A quasi-standing wave field is present in front of the vertical-wall harbour structure embodying the OWC. The characteristics of the quasi-standing wave field depend on the radiated and reflected wave heights and on the phase difference between incident and reflected plus radiated wave trains. Minimum values of the ratio of the quasi-antinode height to the incident wave height H_v/H = 1.1 are found.

Based on dimensional analysis of the dataset obtained in this work, empirical prediction formulae are developed for K_{rr} and H_v/H. These formulae could be used for design purpose in harbour engineering practice.

Declaration of competing interest

The authors declare that they have no known competing financial interests or personal relationships that could have appeared to influence the work reported in this paper.

Acknowledgements

This research did not receive any specific grant from funding agencies in the public, commercial, or not-for-profit sectors.

Appendix A. Sensitivity tests on wave reflection from a vertical wall

The performance of *interFoam* solver of OpenFOAM® in simulating the propagation of highly non-linear waves was assessed by Larsen et al. (2019). Such work demonstrated the importance of an accurate choice of the spatial resolution, but also proved the fundamental effect of the adopted discretization schemes and Courant number (Co), including the Courant number at the air-water interface (αCo). These aspects are particularly important to ensure the stability of wave propagation in long-term simulations, which were found to be challenging for *interFoam* solver. Therefore, a sensitivity analysis for wave propagation in the empty NWT with a 40 m length is performed, aimed at assessing the reflection from a vertical wall and to estimate the numerical wave damping taking place during wave propagation. Waves are generated with the *waves2foam* toolbox, using release 1712 of OpenFOAM®. The reflection coefficient K_{rr} is estimated with the methodology described in *section 2.2*. The sensitivity to the following factors is evaluated:

(i) the turbulence model (comparing the standard k-ω SST model, the *buoyancy-modified* k-ω SST model presented by Devolder et al. (2017) and the simulation performed by assuming laminar flow conditions);
(ii) the time step (considering different *Co* and *αCo* values);
(iii) the discretization scheme for time marching solutions (*ddt-scheme*). The following schemes of OpenFOAM® are compared: *Euler* (a first-order forward Euler scheme), *CrankNicolson* (CN), which includes a blending factor ψ and corresponds to a pure Crank Nicolson second-order scheme for $\psi = 1$ and to a pure Euler scheme for $\psi = 0$.

In the sensitivity analysis performed here, the grid resolution is kept constant and equal to H/cell = 20 and L/cells = 300. Such resolution was proved to be sufficient to achieve substantially grid-independent results in previously performed studies (Cappietti and Simonetti, 2018).

The observed errors possibly leading to inaccuracies in wave propagations are two-fold: on one side, when relatively large Courant numbers are used, a non-physical increase of the wave steepness (with an increase of wave height) and non-linearity is observed while the wave progresses in space, as previously observed in the literature (Larsen et al., 2019). This effect results in values of the reflection coefficient $K_{rr}>1$ for some numerical set-up (Table A1), which is present regardless of the turbulence model used (being particularly evident in the laminar flow case). On the other side, for a fixed position in space, a progressive numerical wave damping (i.e. an increase in the diffusive error) in time is observed when the standard k-ω SST model is used (Fig. A1).

To obtain a stable wave propagation in the NWT, the following numerical set-up was used in the present work: the *buoyancy-modified* k-ω SST model is used, with *Co* and $\alpha Co = 0.2$ and a *CrankNicolson* with $\psi = 0.9$ time discretization scheme.

Table A.1
Reflection coefficient from a vertical wall K_{rr} obtained with *interFoam* solver and *waves2Foam* wave generation toolbox for different temporal resolution (*Co* and *αCo*), discretization scheme (*ddt-scheme*) and turbulence modelling.

	buoyancy-modified k-ω SST	standard k-ω SST	laminar
	Reflection coefficient K_{rr}		
Co, αCo = 0.2 - Euler	0.92	0.96	0.97
Co, αCo = 0.2 - CN, $\psi = 0.2$	0.95	0.98	1.01
Co, αCo = 0.2 - CN, $\psi = 0.5$	1.05	0.99	1.03
Co, αCo = 0.2 - CN, $\psi = 0.9$	0.99	0.98	1.03
Co, αCo = 0.1 - CN, $\psi = 0.9$	0.97	0.99	1.01
Co, αCo = 0.2 - CN, $\psi = 0.9$	0.99	0.98	1.03
Co, αCo = 0.4 - CN, $\psi = 0.9$	1.03	0.98	1.04
Co, αCo =0.6 - CN, $\psi = 0.9$	1.07	0.99	1.06
Co, αCo =0.8 - CN, $\psi = 0.9$	1.07	1.04	1.07

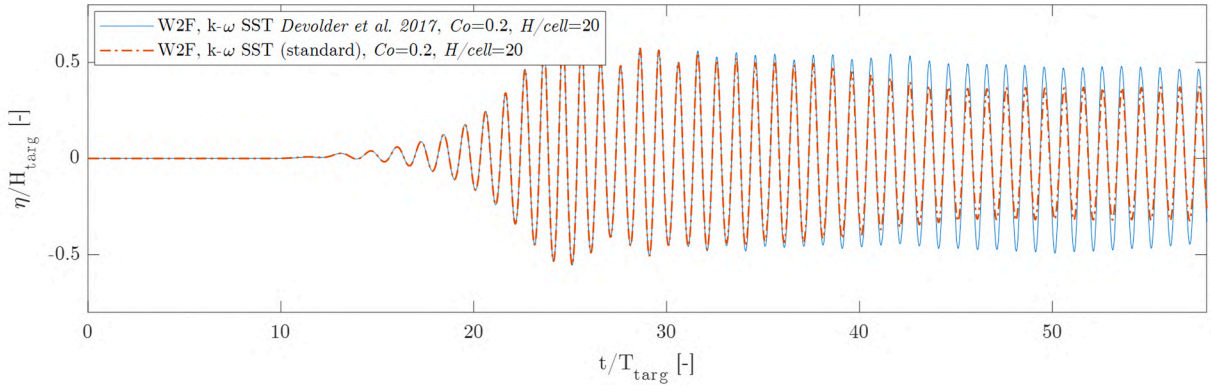

Fig. A.1. Simulated surface elevation as a function of time obtained with waves2Foam using the k-ω SST model in the standard version and in the buoyancy-modified version (Devolder et al., 2017). Fixed parameters: H/cells = 20, Co = 0.2, *ddt-scheme*: CrankNicolson (CN) with blending factor $\psi = 0.9$. Results at a distance from wave generation equal to 15 wavelengths L.

Appendix B. Exemplary evaluation of the OWC resonance frequency

As a first approximation, the resonant frequency of an OWC structure can be estimated from the draught of its front wall (D) utilizing analytical relations (Evans and Porter, 1995; McCormick, 2007). Following McCormick (2007), the resonant frequency of the structure f_{owc} can be expressed as in Eq. (B.1):

$$f_{owc} = \frac{1}{2\pi}\sqrt{\frac{g}{D + D_a}} \tag{B.1}$$

where D_a is an additional length due to the added mass of the system, here assumed equal to D, as in (Vyzikas et al., 2017). To support the discussion of the effect of D/H on K_{rad} in *section 4.2* (Fig. 12), Eq. B.1 is exemplarily applied to evaluate the resonant frequency of the OWC configurations with $D/H = 3.3$, 2.5 and 1.7 and $kh = 1.58$, $V/W = 0.05$, $W/L = 0.08$ (Tab. B1). For these configurations, the incident wave f_{wave} is always smaller than the estimated resonant frequency of the structure, f_{owc}. In this conditions, an increase in the value of D/H (hence, an increase of D for a fixed value of the incident wave height H) causes the device to work closer to resonance, determining higher capture width ratios CW and radiation coefficients K_{rad}.

Table B.1
OWC geometry parameters and wave conditions (at model scale 1:15), dimensionless parameters and OWC resonant frequency (f_{owc}) analytically estimated for different exemplary configurations tested.

D [m]	W [m]	V [m]	H [m]	f_{wave} [Hz]	kh [−]	D/H [−]	W/L [−]	V/W [−]	f_{owc} [Hz]
0.133	0.2	0.01	0.04	0.77	1.58	3.3	0.08	0.05	0.97
0.100	0.2	0.01	0.04	0.77	1.58	2.5	0.08	0.05	1.11
0.067	0.2	0.01	0.04	0.77	1.58	1.7	0.08	0.05	1.36

References

Altomare, C., Gironella, X., 2014. An experimental study on scale effects in wave reflection of low-reflective quay walls with internal rubble mound for regular and random waves. Coast. Eng. 90, 51–63. https://doi.org/10.1016/j.coastaleng.2014.04.002.

Altomare, C., Gironella, X., Sospedra, J., 2013. Wave reflection: small and large scale experiments on wave absorbing quay walls. In: Coasts, Mar. Struct. Break. 2013 from Sea to Shore - Meet. Challenges Sea, pp. 1409–1417.

Arena, F., Malara, G., Romolo, A., 2014. A U-OWC wave energy converter in the Mediterranean sea: preliminary results on the monitoring system of the first prototype. In: Renew. Energies Offshore - 1st Int. Conf. Renew. Energies Offshore. https://doi.org/10.1201/b18973-59. RENEW.

Brendmo, A., Falnes, J., Lillebekken, P.M., 1996. Linear modelling of OWC including viscous loss. Appl. Ocean Res. 18, 65–75.

Cappietti, L., Simonetti, I., 2018. On the effectiveness of oscillating water column devices in reducing the agitation in front of vertical walls harbor structures. Proc. Coast. Eng. Conf. 36, 1–12. https://doi.org/10.9753/icce.v36.structures.67.

Cavallaro, L., Faraci, C., Foti, E., Musumeci, R.E., Scandura, P., 2009. An experimental comparative analysis on wave reflection of two types of caissons. World Scientific Pub Co Pte Lt, pp. 1035–1046. https://doi.org/10.1142/9789814282024_0091.

Ciocan, C.S., Taveira-Pinto, F., das Neves, L., Rosa-Santos, P., 2017. Experimental study of the hydraulic efficiency of a novel perforated-wall caisson concept, the LOWREB. Coast. Eng. 126, 69–80. https://doi.org/10.1016/j.coastaleng.2017.06.001.

Crema, I., Simonetti, I., Cappietti, L., Oumeraci, H., 2015. Laboratory experiments on oscillating water column wave energy converters integrated in a very large floating structure. In: 11th Wave Tidal Energy Conf. EWTEC2015. Nantes, France, p. 8.

Devolder, B., Rauwoens, P., Troch, P., 2017. Application of a buoyancy-modified k-ω SST turbulence model to simulate wave run-up around a monopile subjected to regular waves using OpenFOAM®. Coast. Eng. 125, 81–94. https://doi.org/10.1016/j.coastaleng.2017.04.004.

Devolder, B., Troch, P., Rauwoens, P., 2018. Performance of a buoyancy-modified k-ω and k-ω SST turbulence model for simulating wave breaking under regular waves using OpenFOAM®. Coast. Eng. 138, 49–65. https://doi.org/10.1016/j.coastaleng.2018.04.011.

Elhanafi, A., Fleming, A., Macfarlane, G., Leong, Z., 2016a. Underwater geometrical impact on the hydrodynamic performance of an offshore oscillating water column–wave energy converter. Renew. Energy 105, 209–231. https://doi.org/10.1016/j.renene.2016.12.039.

Elhanafi, A., Fleming, A., Macfarlane, G., Leong, Z., 2016b. Numerical energy balance analysis for an onshore oscillating water column–wave energy converter. Energy 116, 539–557. https://doi.org/10.1016/j.energy.2016.09.118.

Elhanafi, A., Fleming, A., Macfarlane, G., Leong, Z., 2017a. Numerical hydrodynamic analysis of an offshore stationery–floating oscillating water column–wave energy converter using CFD. Int. J. Nav. Archit. Ocean Eng. 9, 77–99. https://doi.org/10.1016/j.ijnaoe.2016.08.002.

Elhanafi, A., Macfarlane, G., Fleming, A., Leong, Z., 2017b. Experimental and numerical investigations on the hydrodynamic performance of a floating–moored oscillating water column wave energy converter. Appl. Energy 205, 369–390. https://doi.org/10.1016/j.apenergy.2017.07.138.

Evans, D.V., Porter, R., 1995. Hydrodynamic characteristics of an oscillating water column device. Appl. Ocean Res. 17, 155–163.

Falcão, A.F.O., Henriques, J.C.C., 2016. Oscillating-water-column wave energy converters and air turbines: a review. Renew. Energy 85, 1391–1424. https://doi.org/10.1016/j.renene.2015.07.086.

Falcão, A.F.O., Sarmento, A.J.N.A., Gato, L.M.C., Brito-Melo, A., 2020. The Pico OWC wave power plant: its lifetime from conception to closure 1986–2018. Appl. Ocean Res. https://doi.org/10.1016/j.apor.2020.102104.

Falcão, A.F.O., Henriques, J.C.C., 2014. Model-prototype similarity of oscillating-water-column wave energy converters. Int. J. Mar. Energy. 6, 18–34. https://doi.org/10.1016/j.ijome.2014.05.002.

Falnes, J., 2002. Ocean Waves and Oscillating Systems. Cambridge University Press.

Faraci, C., Scandura, P., Foti, E., 2015. Reflection of sea waves by combined caissons. J. Waterw. Port, Coast. Ocean Eng. 141, 1–12. https://doi.org/10.1061/(ASCE)WW.1943-5460.0000275.

Fugazza, M., Natale, L., 1992. Hydraulic design of perforated breakwaters. J. Waterw. Port, Coast. Ocean Eng. 118, 1–14. https://doi.org/10.1061/(ASCE)0733-950X, 118: 1(1).

Fuhrman, D.R., Larsen, B.E., 2019. A discussion on "Numerical computations of resonant sloshing using the modified isoAdvector method and the buoyancy-modified turbulence closure model". Appl. Ocean Res. 93 (2020), 101829, 10.1016.j.apor.2019.05.014.

Garrido, J.M., Ponce De León, D., Berruguete, A., Martínez, S., Manuel, J., Fort, L., Yagüe, D., González-Escrivá, J.A., Medina, J.R., 2010. Study of reflection of new low-reflectivity quay wall caisson. Proc. Coast. Eng. Conf.

Goda, Y., Suzuki, Y., 1977. Estimation of incident and reflected waves in random wave experiments. 15th Int. Conf. Coast. Eng., pp. 828–845

Gonzalez-Escriva, J.A., Medina, J.R., 2012. Antireflective Vertical Structure Extended for attenuation of low frequency waves. Int. Conf. Costal Eng. 1–9.

Gurnari, L., Filianoti, P.G.F., Torresi, M., Camporeale, S.M., 2020. The wave-to-wire energy conversion process for a fixed U-OWC device. Energies 13, 1–25. https://doi.org/10.3390/en13010283.

He, F., Huang, Z., 2016. Using an oscillating water column structure to reduce wave reflection from a vertical wall. J. Waterw. Port, Coast. Ocean Eng. 142, 1–10. https://doi.org/10.1061/(ASCE)WW.1943-5460.0000320.

He, F., Li, M., Huang, Z., 2016. An experimental study of pile-supported OWC-type breakwaters: energy extraction and vortex-induced energy loss. Energies 9, 540. https://doi.org/10.3390/en9070540.

Healy, J.J., 1951. Wave damping effect of beaches. In: Minnesota Int. Hydraul. Conv., pp. 213–220.

Hirt, C., Nichols, B., 1981. Volume of Fluid (VOF) method for the dynamics of free boundaries. J. Comput. Phys. 39, 201–225. https://doi.org/10.1016/0021-9991(81)90145-5.

Howe, D., Nader, J.R., 2017. OWC WEC integrated within a breakwater versus isolated: experimental and numerical theoretical study. Int. J. Mar. Energy. 20, 165–182. https://doi.org/10.1016/j.ijome.2017.07.008.

Huang, Z., Li, Y., Liu, Y., 2011. Hydraulic performance and wave loadings of perforated/slotted coastal structures: a review. Ocean Eng. 38, 1031–1053. https://doi.org/10.1016/j.oceaneng.2011.03.002.

Iturrioz, A., Guanche, R., Lara, J.L., Vidal, C., Losada, I.J., 2015. Validation of OpenFOAM® for oscillating water column three-dimensional modeling. Ocean Eng. 107, 222–236. https://doi.org/10.1016/j.oceaneng.2015.07.051.

Jacobsen, N.G., Fuhrman, D.R., Fredsøe, J., 2012. A wave generation toolbox for the open-source CFD library: OpenFoam®. Int. J. Numer. Methods Fluid. 70, 1073–1088. https://doi.org/10.1002/fld.2726.

Jarlan, G.E., 1961. A perforated vertical wall breakwater. Dock Harbour Auth. 41.

Jasak, H., 1996. Error Analysis and Estimation for the Finite Volume Method with Applications to Fluid Flows. University of London. https://doi.org/10.1016/S0020-7683(02)00168-3.

Larsen, B.E., Fuhrman, D.R., 2018. On the over-production of turbulence beneath surface waves in Reynolds-averaged Navier-Stokes models. J. Fluid Mech. 853, 419–460. https://doi.org/10.1017/jfm.2018.577.

Larsen, B.E., Fuhrman, D.R., Roenby, J., 2019. Performance of interFoam on the simulation of progressive waves. Coast Eng. J. 61, 380–400. https://doi.org/10.1080/21664250.2019.1609713.

Lee, J.I., Shin, S., 2014. Experimental study on the wave reflection of partially perforated wall caissons with single and double chambers. Ocean Eng. 91, 1–10. https://doi.org/10.1016/j.oceaneng.2014.08.008.

Lopez, I., Pereiras, B., Castro, F., Iglesias, G., 2014. Optimisation of turbine-induced damping for an OWC wave energy converter using a RANS-VOF numerical model. Appl. Energy 127, 105–114. https://doi.org/10.1016/j.apenergy.2014.04.020.

López, I., Rosa-Santos, P., Moreira, C., Taveira-Pinto, F., 2018. RANS-VOF modelling of the hydraulic performance of the LOWREB caisson. Coast. Eng. 140, 161–174. https://doi.org/10.1016/j.coastaleng.2018.07.006.

López, I., Carballo, R., Iglesias, G., 2019. Site-specific wave energy conversion performance of an oscillating water column device. Energy Convers. Manag. 195, 457–465. https://doi.org/10.1016/j.enconman.2019.05.030.

López, I., Carballo, R., Taveira-Pinto, F., Iglesias, G., 2020. Sensitivity of OWC performance to air compressibility. Renew. Energy 145, 1334–1347. https://doi.org/10.1016/j.renene.2019.06.076.

Mansard, E.P.D., Funke, E.R., 1980. The measurement of incident and reflected spectra using a least squares method. In: Coast. Eng. 1980. American Society of Civil Engineers, New York, NY, pp. 154–172. https://doi.org/10.1061/9780872622647.008.

Martins-Rivas, H., Mei, C.C., 2009. Wave power extraction from an oscillating water column at the tip of a breakwater. J. Fluid Mech. 626, 395–414. https://doi.org/10.1017/S0022112009005990.

Masuda, Y., 1971. Wave activated generator for robot weather buoy and other use. Bordeaux, France. In: Colloq. Int. Sur l'Exploitation Des Ocean..

McCormick, M.E., 2007. Ocean Wave Energy Conversion. Dover Publications.

Mei, C.C., 2012. Hydrodynamic principles of wave power extraction. Philos. Trans. R. Soc. A Math. Phys. Eng. Sci. 370, 208–234. https://doi.org/10.1098/rsta.2011.0178.

Menter, F., 1992. Improved two-equation k-omega turbulence models for aerodynamic flows. NASA Tech. Memo. 1–31.

Mustapa, M.A., Yaakob, O.B., Ahmed, Y.M., Rheem, C.K., Koh, K.K., Adnan, F.A., 2017. Wave energy device and breakwater integration: a review. Renew. Sustain. Energy Rev. 77, 43–58. https://doi.org/10.1016/j.rser.2017.03.110.

Naty, S., Viviano, A., Foti, E., 2016. Wave energy exploitation system integrated in the coastal structure of a Mediterranean port. Sustain. Times 8. https://doi.org/10.3390/su8121342.

Neelamani, S., Al-Salem, K., Taqi, A., 2017. Experimental investigation on wave reflection characteristics of slotted vertical barriers with an impermeable back wall in random wave fields. J. Waterw. Port, Coast. Ocean Eng. 143, 1–10. https://doi.org/10.1061/(ASCE)WW.1943-5460.0000395.

Ning, D., Wang, R., Zou, Q., Teng, B., 2016. An experimental investigation of hydrodynamics of a fixed OWC Wave Energy Converter. Appl. Energy 168, 636–648. https://doi.org/10.1016/j.apenergy.2016.01.107.

Oumeraci, H., 2008. Nonconventional wave damping structures: hydraulic performance. In: Kim, Y.C. (Ed.), Coast. Eng. 2008. World Scientific Publishing Company, pp. 3496–3508.

Paulsen, B.T., Bredmose, H., Bingham, H.B., Jacobsen, N.G., 2014. Forcing of a bottom-mounted circular cylinder by steep regular water waves at finite depth. J. Fluid Mech. 755, 1–34. https://doi.org/10.1017/jfm.2014.386.

Robinson, R.N., Murray, A., 1981. Geometric-wavefield influence on the behaviour of an oscillating water column. In: Proc. Int. Syrup. Hydrodyn. Ocean Eng. Norwegian Inst. of Tech., pp. 1067–1086

Sarmento, A.J.N.A., 1993. Model tests optimization of an OWC wave power plant. Int. J. Offshore Polar Eng. 3, 66–72.

Sarmento, A.J.N.A., Falcão, A.F. de O., 1985. Wave generation by an oscillating surface-pressure and its application in wave-energy extraction. J. Fluid Mech. 150, 467–485. https://doi.org/10.1017/S0022112085000234.

Scarpetta, F., Gurnari, L., Torresi, M., Filianoti, P., Camporeale, S., 2017. A CFD simulation of a full scale U-OWC breakwater. Proc. Twelfth Eur. Wave Tidal Energy Conf.

Sheng, W., Lewis, T., Alcorn, R., 2012. On wave energy extraction of oscillating water column device. 4th Int. Conf. Ocean Energy, Dublin, Ireland, p. 9.

Simonetti, I., Cappietti, L., Elsafti, H., Oumeraci, H., 2017. Optimization of the geometry and the turbine induced damping for fixed detached and asymmetric OWC devices: a numerical study. Energy 139, 1197–1209. https://doi.org/10.1016/j.energy.2017.08.033.

Simonetti, I., Cappietti, L., Elsafti, H., Oumeraci, H., 2018. Evaluation of air compressibility effects on the performance of fixed OWC wave energy converters using CFD modelling. Renew. Energy 119, 741–753. https://doi.org/10.1016/j.renene.2017.12.027.

Theocharis, I., Anastasaki, E.N., Moutzouris, C.I., Giantsi, T., 2011. A new wave absorbing quay-wall for wave height reduction in a harbor basin. Ocean Eng. 38, 1967–1978. https://doi.org/10.1016/j.oceaneng.2011.09.020.

Torre-Enciso, Y., Ortubia, I., De Aguileta, L.I.L., Marqués, J., 2009. Mutriku wave power Plant : from the thinking out to the reality. In: 8th Eur. Wave Tidal Energy Conf., pp. 319–329. Uppsala, Sweden.

Vicinanza, D., Di Lauro, E., Contestabile, P., Gisonni, C., Lara, J.L., Losada, I.J., 2019. Review of innovative harbor breakwaters for wave-energy conversion. J. Waterw. Port, Coast. Ocean Eng. 145, 1–18. https://doi.org/10.1061/(ASCE)WW.1943-5460.0000519.

Viviano, A., Naty, S., Foti, E., Bruce, T., Allsop, W., Vicinanza, D., 2016. Large-scale experiments on the behaviour of a generalised Oscillating Water Column under random waves. Renew. Energy 99, 875–887. https://doi.org/10.1016/j.renene.2016.07.067.

Viviano, A., Musumeci, R.E., Vicinanza, D., Foti, E., 2019. Pressures induced by regular waves on a large scale OWC. Coast. Eng. 152, 103528. https://doi.org/10.1016/j.coastaleng.2019.103528.

Vyzikas, T., Deshoulières, S., Barton, M., Giroux, O., Greaves, D., Simmonds, D., 2017. Experimental investigation of different geometries of fixed oscillating water column devices. Renew. Energy 104, 248–258. https://doi.org/10.1016/j.renene.2016.11.061.

Weber, J.W., 2007. Representation of non-linear aero-thermodynamic effects during small scale physical modelling of OWC WECs. In: Proc. 7th Eur. Wave Tidal Energy Conf. Porto. Port.

Windt, C., Davidson, J., Ringwood, J.V., 2018. High-fidelity numerical modelling of ocean wave energy systems: a review of computational fluid dynamics-based numerical wave tanks. Renew. Sustain. Energy Rev. 93, 610–630. https://doi.org/10.1016/j.rser.2018.05.020.

Zabihi, M., Mazaheri, S., Montazeri, M., 2019. Experimental hydrodynamic investigation of a fixed off shore Oscillating Water Column device, 85, 20-33. https://doi.org/10.1016/j.apor.2019.01.036.

Zhu, S., Chwang, A.T., . Investigations on the reflection behaviour of a slotted seawall. Coast. Eng. 43, 93–104. https://doi.org/10.1016/S0378-3839(01)00008-4.